APPLIED PHYSICS

Optimal control pulses for the 1.2-GHz (28.2-T) NMR spectrometers

David Joseph and Christian Griesinger*

The ability to measure nuclear magnetic resonance (NMR) spectra with a large sample volume is crucial for concentration-limited biological samples to attain adequate signal-to-noise (S/N) ratio. The possibility to measure with a 5-mm cryoprobe is currently absent at the 1.2-GHz NMR instruments due to the exceedingly high radio frequency power demands, which is four times compared to 600-MHz instruments. Here, we overcome the high-power demands by designing optimal control (OC) pulses with up to 20 times lower power requirements than currently necessary at a 1.2-GHz spectrometer. We show that multidimensional biomolecular NMR experiments constructed using these OC pulses can bestow improvement in the S/N ratio of up to 26%. With the expected power limitations of a 5-mm cryoprobe, we observe an enhancement in the S/N ratio of more than 240% using our OC sequences. This motivates the development of a cryoprobe with a larger volume than the current 3-mm cryoprobes.

INTRODUCTION

Nuclear magnetic resonance (NMR) spectroscopy relies on the magnetic moments of nuclei with spin quantum number $m_s > 0$ (*1*, *2*) (commonly and for this work: $m_s = ½$) to obtain atomic resolution information that is useful to determine the structure and dynamics of molecules as well as their interactions (*3*). Thus, the technique provides a unique atomic-level probe to investigate biological macromolecules such as proteins (*4*–*9*), enzymes (*10*), RNA (*11*, *12*), and DNA (*13*, *14*) in their native physiologically relevant states (*15*, *16*), which in turn assists to solve a large variety of biological questions. One of the major bottlenecks in such NMR studies is the inherent limitation on the sensitivity due to the very small energy difference between the spin states (*3*, *17*). On top of this, many interesting biological systems such as the intrinsically disordered proteins (IDPs) (*16*), in-cell samples (*15*), and metabolic samples (*18*) will have little dispersion in the NMR resonance frequencies of different homonuclear spins. This peak crowding limits the analysis of NMR spectra. Because the energy difference between the two states is proportional to the external magnetic field (B_0), by increasing this field one can improve the sensitivity by $B_0^{3/2}$ (*3*). This increased external magnetic field also increases the dispersion of crowded peaks proportional to B_0^n, where n is the number of dimensions of the NMR experiment (*1*). Thus, the recent availability of commercial ultrahigh-field 1.2-GHz (28.2-T) (*19*, *20*) NMR spectrometers with its increased sensitivity and dispersion broadens the scope for studying increasingly complex biological systems (*21*–*23*).

The sensitivity at 1.2 GHz will be improved by a factor of $2^{1.5}$, which is almost three times compared to a 600-MHz spectrometer (fig. S1). One also observes a larger chemical shift dispersion for proton resonances at 1.2 GHz, and this is true for most nuclei of interest in biological NMR where field-independent dipolar relaxation dominates over chemical shift anisotropy-induced relaxation. Thus, at 1.2 GHz, for the ^{1}H nuclei a 10-ppm (parts per million) window corresponds to 12 kHz, for the ^{15}N nuclei a 40-ppm window corresponds to ≈4.8 kHz, and for the ^{13}C nuclei a 200-ppm window corresponds to ≈60 kHz, implying that we see an improved dispersion in all the NMR experiments. Unfortunately, to achieve uniform rotation of the spins dispersed in such large frequency ranges, we require broadband pulses (*24*) during an NMR experiment. If we scale the pulses with the B_0 field, the commonly used hard pulses would be shorter by half compared to a 600-MHz spectrometer. Hence, such a broadband 90° pulse on a 1.2-GHz spectrometer would require twice the radio frequency (RF) amplitude or four times the power. In principle, one should be able to increase the RF power to achieve the required spin state transformation in these large frequency windows as long as the sample is intact. However, the maximum power available for an NMR experiment is strictly limited by the power handing capability of the current probes, which is particularly limited for cryogenically cooled probes (or cryoprobes) (*25*, *26*) that are essential to obtain sufficient S/N ratio, especially in concentration-limited biological samples. The limited RF power tolerance thus requires low-power pulses for the cryoprobes at ultrahigh-field 1.2-GHz spectrometers. The immediate implication of using low-power RF pulses is the well-known off-resonance effect (*3*), leading to offset-dependent deviation from the desired rotation of spins, resulting in incomplete coherence transfer (*3*) between spins at distant offsets. This then translates as a loss of sensitivity and, given the short phase cycles (*3*) in multidimensional NMR experiments, as artifacts in the NMR spectra, thus leading to incorrect or incomplete interpretation of the NMR spectra. This problem can be avoided by reducing the sample diameter and the sample volume (*27*), hence permitting to reduce coil diameter of the cryogenically cooled probe. The RF coil with a smaller diameter can generate adequate RF amplitude or B_1 field (*28*) to facilitate uniform excitation of a large bandwidth using a tolerated power. At present, this limitation is visible for the ultrahigh-field magnets, and for the above reason, the commercial manufacturer of 1.2-GHz spectrometers (Bruker) provides only a 3-mm cryoprobe optimized for proton detection (inverse cryoprobe), limiting the maximum sample volume to approximately 100 μl. This is a serious limitation for studying concentration-limited samples

Max Planck Institute for Multidisciplinary Sciences, Göttingen, Niedersachsen D-37077, Germany.
*Corresponding author. Email: cigr@mpinat.mpg.de

such as some IDPs, large complexes, membrane proteins in micelles, in-cell samples, and metabolic samples, where measuring on a 5-mm cryoprobe with a larger sample volume (250 μl in a Shigemi tube) would have the potential of an additional improvement in the S/N ratio (*2*, *3*). Furthermore, the abovementioned power limitation would become even more critical for studying biological samples that have high salt concentrations, which are required for the stability of the biological macromolecules. These large salt concentrations make the RF pulses even longer (*29*) on the cryoprobes, aggravating the difficulties in implementing broadband pulses. To fully exploit the maximum sensitivity achievable at our 1.2-GHz spectrometer, we are expecting such a 5-mm inverse cryoprobe from Bruker to be installed at our facility in the near future for studying concentration-limited samples. As a motivation to build such a 5-mm inverse cryoprobe probe, we try to understand the performance of RF amplitude–limited pulses for biomolecular NMR experiments. We restrict the maximum RF amplitude to 20 kHz on the ^{1}H, 15 kHz on the ^{13}C, and 5.6 kHz on the ^{15}N channels to simulate such an RF power–restricted cryoprobe.

The problem of accomplishing maximum transfer with limited power availability is an optimal control (OC) problem (*30*–*36*). OC theory was introduced to NMR spectroscopy two decades ago as gradient ascent pulse engineering (GRAPE) (*37*, *38*) algorithm, which is a general method for pulse design. The GRAPE method aims at optimizing RF pulse shapes [controls or $c^{(k)}(t)$] by maximizing a cost or fidelity function $\Phi[c^{(k)}(t)]$, that is, to maximize the real part of the overlap between a desired target density operator state and the resulting density operator state after applying the controls or the pulse shape

$$\Phi[c^{(k)}(t)] = Re\langle\sigma_{\text{targ}}|\exp\{-i\int_o^T[\hat{\text{H}}^{(0)} + \sum_k c^{(k)}(t)\hat{\text{H}}^{(\text{k})}]dt\}|\sigma_0\rangle \quad (1)$$

where σ_{targ} is the desired target density operator state, σ_0 is the initial density operator state, $\hat{\text{H}}^{(0)}$ is the system Hamiltonian (drift), and $\hat{\text{H}}^{(\text{k})}$ are the control Hamiltonians. The algorithm proceeds to find the maximum for the fidelity function by varying the controls in the direction of the function derivative $\frac{\partial\Phi[c^{(k)}(t)]}{\partial c_n^{(k)}}$ until one of the exit criteria is reached (*39*), where $c_n^{(k)}$ is the *n*th control after a piecewise-constant approximation of Eq. 1. This procedure was extremely effective in optimizing broadband excitation (*40*–*42*), inversion (*41*, *42*), and refocusing pulses (*43*) that had limited RF amplitude (*44*) and large B_1 miscalibration (*45*). An improved version of the GRAPE method has also been efficiently implemented in the MATLAB-based open source package Spinach (*46*) as limited-memory Fletcher-Goldfarb-Shanno algorithm (L-BFGS) (*47*–*49*), which we used to generate our pulse shapes. The GRAPE method has been extensively used for small-molecule pulse sequences (*50*–*53*) and had applications in bio-NMR experiments such as for homonuclear (*54*) and broadband decoupling pulses (*55*), as robust inversion pulses in the NOESY-HMQC (nuclear Overhauser effect spectroscopy with heteronuclear multiple quantum coherence) experiment (*24*), and for band-selective pulse design (*56*, *57*). In solid-state NMR, the GRAPE algorithm has been successfully used for designing improved OC cross-polarization schemes (*58*–*61*). Inspired by the success of the GRAPE algorithm in NMR spectroscopy, OC-based laser pulse design (*62*–*64*) is also used for atom interferometry.

The bulk of the pulsed Fourier transform NMR experiments require two common RF pulses that rotate spins through either 90° or 180° angles and are essential for building elementary blocks (*3*) that achieve the desired coherence transfer [e.g., insensitive nuclei enhanced by polarization transfer (INEPT) (*65*), constant time evolution (*3*), and multiple quantum generation block (*3*)]. In these elementary blocks, the 90° RF pulse is used for excitation and a 180° RF pulse is used for either inversion or refocusing of the spin magnetization vector. To achieve the maximum performance during each coherence transfer block, the abovementioned high-power rectangular pulses need to have the ability to uniformly rotate spins from all the involved nuclei that are spread across a range of frequencies or bandwidth. This is not true for rectangular pulses with limited RF amplitude where the well-known offset or off-resonance effect becomes marked as one goes to higher and higher field NMR spectrometers. Figure S1 (A and B) shows one-dimensional (1D)–^{1}H NMR spectra of the ubiquitin protein with two different RF amplitudes at two different magnetic field strengths. We observe that in agreement with our expectation, a low-power pulse with an RF amplitude of 8.5 kHz (which is the expected maximum RF amplitude value on the 5-mm cryoprobe for a sample with 3 mM salt) leads to a marked reduction of intensity at the farthest offset at 1.2 GHz compared to 600 MHz. We observe that the low-power rectangular pulses are inefficient due to the imperfections contributed by the off-resonance effects and B_1 inhomogeneity. These imperfections can accumulate and lead to substantial signal loss in multipulse experiments. Hence, compensating for such imperfections is mandatory for pulse sequence development, especially at high fields (*3*).

We choose to use low-power universal rotation (UR)–90° and UR-180° pulses because they can serve as basic building blocks for constructing most of the solution NMR experiments. The UR pulses (*43*) control all the three orthogonal Cartesian components of the macroscopic magnetization vector; hence, they are costlier than the point-to-point (PP) (*41*, *42*) transformations, which control only one of the Cartesian components of the magnetization vector. There have been extensive studies in the past on designing robust UR pulses using the OC theory; they are known as broadband universal rotation by optimized pulses (*43*). These UR pulses can be thought of as idealized pulses that perform the desired unitary rotation of the macroscopic magnetization vector within an offset range and the B_1 field deviations of interest in an NMR sample. Hence, a set of UR pulses can serve as a direct replacement element for each of the hard pulse in a sequence. We are interested in constructing pulses that covered a minimum bandwidth of 15 kHz (12.5 ppm) with an RF amplitude less than 20.2 kHz on the ^{1}H channel and a bandwidth of 6 kHz (50 ppm) for the ^{15}N channel with an RF amplitude less than 5.6 kHz on the ^{15}N channel. Because higher salt concentration in an NMR sample will reduce the achievable RF amplitudes (*29*), we wish to generate pulses with the lowest possible RF amplitudes, ideally less than 10 kHz on the ^{1}H channel and less than or equal to 5 kHz on the ^{15}N channel. In addition, we aim for pulses that are tolerant to B_1 inhomogeneity of not less than ±15% to have faithful experimental reproducibility (*66*). Earlier studies exploring the limits of UR pulses have shown that for a given RF amplitude, longer pulse durations are required to cover a larger bandwidth and to tolerate higher B_1

inhomogeneity ranges (*43*). One could, in principle, design pulse shapes with longer durations that have substantially lower RF amplitudes than our threshold values. Unfortunately, longer UR pulses in the experiments for biological macromolecules will lead to a loss in the S/N ratio due to the fast transverse relaxation (*3*) in these macromolecules. Hence, as an additional constraint, we decided to use pulses that had a maximum pulse duration of 700 μs to limit the relaxation losses. We show that robust UR pulses that obey the low-power constraints can be designed for constructing bio-NMR experiments. We also study the transfer efficacy of such individual elemental UR pulses in detail and the performance of a set of 2D bio-NMR experiments constructed using these pulses.

Furthermore, most NMR experiments with three or more dimensions involving the ^{13}C nuclei require selective manipulations (*67*) that differentiate between the types of ^{13}C atoms [CO, C_α, C-aliphatic (C_{ali}), etc.] based on the desired correlation (or the atom type connectivity) we wish to achieve in a particular multidimensional experiment (*3*, *67*). The established way to realize this is by using the band-selective Gaussian cascade pulses (*68*–*70*). These pulses follow the excitation profile scheme (*70*) shown in fig. S1C, where a selected band or region is excited, the signals far from this band are minimized or suppressed (suppression band), and the above two regions are separated by a transition band. It is observed that the Gaussian cascade pulses reach the allowed threshold for permissible RF power values already at 800 MHz (18.8 T) and larger frequencies or fields. As an example, the Q3.1000 (*69*) pulse when used for refocusing C_{ali} spins that are over the bandwidth of 16 kHz would require an RF amplitude of 22.7 kHz on an 800-MHz spectrometer. The band-selective Q3.1000 pulse is generated from a superposition of three Gaussians, and the offset dependence was optimized using the Quaternion elements for the UR with 1000 steps in the shape (*69*). A maximum RF amplitude of 15 kHz is expected to be achievable on the ^{13}C channel of a 5-mm inverse cryoprobe at 1.2 GHz. Thus, undoubtedly, these shaped pulses are not suitable to be used at ultrahigh-field magnets, where they usually fail to meet the performance requirements with the RF powers tolerated by the cryoprobes. We were interested in generating shaped pulses that cover a minimum of 9 kHz (30 ppm at 1.2 GHz) for the CO spins, 12 kHz (40 ppm at 1.2 GHz) for the C_α spins, and crucially at least 24 kHz (80 ppm at 1.2 GHz) for the C_{ali} spins. In addition, the duration of these pulses should not exceed the value required by the Gaussian cascade pulses currently used at 1.2 GHz. This is a maximum duration of 380 μs when we have to limit the RF amplitude to 15 kHz. These pulses should be tolerant to B_1 inhomogeneity of at least ±15% to obtain robust experimental reproducibility. To meet the above constraints, we develop a multiband-selective pulse scheme that achieves different arbitrary nutation angles within each of these bands. We also show that improved 3D bio-NMR experiments can be realized for 1.2 GHz using the OC pulses we developed.

In this work, we aim to design low-power OC-based biomolecular solution NMR pulse sequences with RF amplitudes lower than what is expected to be possible on a power-limited 5-mm inverse cryoprobe for a 1.2-GHz spectrometer. We design a set of low-power UR pulses for 90° or 180° transformations of the ^1H and ^{15}N nuclei. A modified OC scheme for multiband selection with multinutation angle using a single pulse is introduced to do two-band differential control (one of them being either a UR-90° or a UR-180° transformation and the other a UR-360° rotation) on two different kinds of ^{13}C nuclei in a protein. These OC pulses were then used for constructing user-friendly low-power versions of the 2D-[^1H,^{15}N]-HSQCs (heteronuclear single quantum coherence spectroscopy) and 2D-[^1H,^{13}C]-TROSY (transverse relaxation optimized spectroscopy) experiments. We also construct triple-resonance 3D-HNCO (experiment that provides correlation between ^{15}N and its attached ^1H and ^{13}C from the CO of previous amino acid, hence the name HNCO) and 3D-TROSY-HNCO experiments. By compensating for B_1 inhomogeneity or miscalibration of up to ±20%, we show that these pulse shapes and thus the OC-pulse sequences are virtually calibration free and that their setup can be easily automated. We demonstrate that these low-power OC-based pulse sequences outperform conventional sequences and are expected to enable large-volume measurements at ultrahigh-field 1.2-GHz NMR spectrometers.

RESULTS

Low-power universal rotation pulses for the ^1H and ^{15}N nuclei

The lack of robust UR pulse that meet the low-power requirements motivated us to search for appropriate pulse shapes using the OC module in Spinach (*46*). We designed a set of UR-90° and UR-180° pulses for both the ^1H and ^{15}N channels by searching for the minimum RF amplitude that can provide a fidelity greater than 0.995 to cover a bandwidth of 15 kHz on ^1H and 6 kHz on ^{15}N. The pulse lengths are restricted to a maximum of 650 μs for the UR-90° pulses and 700 μs for the UR-180° pulses, and both rotations aimed for a B_1 inhomogeneity compensation greater than ±15%. We evaluated the set of solutions obtained first with a simulated 2D excitation profile and second by recording an experimental 2D excitation profile to select for the best pulse shape solution. We observed that with the low-power criterion, the GRAPE optimization did not benefit from the freedom to do amplitude modulation. Such a choice resulted in shapes that had a constant RF amplitude close to the maximum allowed value for most of the pulse duration. Hence, we decided to fix the amplitude to the maximum allowed value and to optimize for phase-modulated UR pulse shapes. The use of phase-modulated shapes would provide an additional benefit for faithfully reproducing the pulse shapes by an arbitrary waveform generator (AWG) when compared to generating an amplitude-modulated shape. To improve the reliability of the phase-modulated shapes, we smoothened them using either a moving average filter or the derivative norm square (DNS) penalty (*71*, *39*) as implemented in Spinach. This allows the AWG to make nonerratic phase jumps and thus permit robust experimental reproducibility (*66*). In addition, we scaled both the ^1H and ^{15}N pulses to identical durations to avoid any undesirable evolution when these pulses are simultaneously applied in a transfer block such as the INEPT block. The details of various parameters used for generating the final set of UR pulse shapes are discussed in Materials and Methods. The final set of UR pulses selected are shown in fig. S2 (A and B) for the UR-90° pulses and in fig. S2 (E and F) for the UR-180° pulses. The UR-90° pulses had a duration of 650 μs, and the UR-180° pulses had a duration of 700 μs for both the ^1H and ^{15}N channels. On the ^1H channel, the pulse shapes cover a bandwidth of ±7.5 kHz with an RF amplitude of 8 kHz, and on the ^{15}N channel, they cover a bandwidth of ±3 kHz with an RF

amplitude of 5 kHz. All the UR pulse shapes were optimized for a B_1 inhomogeneity compensation of ±20%.

The desired transfer of a UR-180° pulse is to convert the vector (I_z, I_x, I_y) to ($-I_z$, I_x, $-I_y$), whereas the UR-90° pulse transfers (I_z, I_x, I_y) vector to ($-I_y$, I_x, I_z) with an efficacy, given by η_{avg} greater than 0.995. Here, η_{avg} is the average transfer efficacy that we used as a performance index to select a robust UR pulse shape. We aimed to retain more than 99.5% of the net transverse magnetization, $|M_{xy}| = \sqrt{M_x^2 + M_y^2}$, after applying the pulse along with a small phase error of ϕ_{avg} less than ±1°. We tested the robustness of our pulses for the desired transfers by simulating the 2D excitation profiles that report the effect of varying the offset and B_1 field. The simulated excitation profiles for the UR-180° pulses that we have designed for ^{1}H and ^{15}N are shown in fig. S3 (B and D). We observe transfer efficacies greater than 0.995 for all the transformations of interest. The only exception was the $-I_y$ to I_y transfer of the UR-180°-^{15}N pulse that had η_{avg} = 0.9938. Fortunately, this value can be accepted because we had a large homogeneous region with transfer efficacy greater than 99%. For comparison, we also show the simulated excitation profiles of the rectangular pulses with the same RF amplitude on top of all the simulated excitation profiles of every UR pulse. It is evident from fig. S3 (A and C) that rectangular pulses of lower RF amplitudes will not achieve the performance necessary at 1.2 GHz. In the case of the UR-90° pulses, we obtain similar robust transfer efficacies with η_{avg} greater than 0.995 for all the transfers except for the I_y to I_z transfer (η_{avg} of 0.9949) of the UR-90°-^{15}N pulse (fig. S4, B and D). We verified the experimental robustness (fig. S5, D to F and J to L) for some of the common transformations that are necessary in an NMR experiment using the above UR pulses. These are the I_z to $-I_y$ transfer for the UR-90° pulses and the $-I_y$ to I_y and I_z to $-I_z$ transfers for the UR-180° pulses. All the above UR pulses did unitary rotations around the x axis with experimental transfer efficacy greater than 0.995 except for the $-I_y$ to I_y transfer of the UR-180°-^{15}N pulse (η_{avg} = 0.9947, which is similar to its simulated performance). We also experimentally observed that none of the low-power rectangular-180° or rectangular-90° pulses have sufficiently large transfer efficacies to execute the desired spin rotations (fig. S5, A to C and G to I) at a 1.2-GHz spectrometer.

We were further interested in decreasing the pulse duration to reduce the transverse relaxation losses for larger biological macromolecules. This was possible by optimizing for pulses with reduced bandwidth of ±6.3 kHz on ^{1}H and ±2.4 kHz on the ^{15}N channel along with a smaller B_1 inhomogeneity compensation of ±15%. An example of such a short UR-180° pulse that had a duration of 540 μs with an RF amplitude of 7.5 kHz, bandwidth coverage of ±6.3 kHz, and B_1 inhomogeneity compensation range of ±15% is shown in Fig. 1A. The robust simulated and experimental performances for the I_y to $-I_y$ transfer of this pulse can be observed from Fig. 1B. We also see that a rectangular pulse of the same RF amplitude has an average transfer efficacy of less than 90% for the above transfer (Fig. 1B). The above UR-180° pulse retained more than 99.5% of the net transverse magnetization and resulted only in a small phase error of ϕ_{avg} less than ±0.15° as observed from Fig. 1C. The set of short pulse shapes is shown in fig. S2 (C and D) for the UR-90° pulses and in fig. S2 (G and H) for the UR-180° pulses. We obtained pulse lengths of 480 μs for the UR-90° pulses and 540 μs for the UR-180° pulses, which is around a 23% reduction in the pulse duration. These shapes also deliver robust transfer efficacies as seen from their simulated and experimental 2D excitation profiles (figs. S6 to S8). The outliers that had slightly lower simulated performance efficacies, that is, η_{avg} less than 0.995, were the I_z to $-I_z$ transfer using the shorter UR-180°-^{15}N pulse (η_{avg} = 0.9945) and the I_x to I_x transfer for the shorter UR-90°-^{1}H pulse (η_{avg}= 0.9947). In the experiment, the I_z to $-I_z$ transfer using a shorter UR-180°-^{15}N pulse had η_{avg} of 0.9932 as seen in fig. S8l, permitting the pulse to be used experimentally. We chose UR shapes that retained a net transverse magnetization $|\mathbf{M_{xy}}|$ greater than 0.995 and resulted only in a small phase error of ϕ_{avg} less than ±0.25° as observed from the simulated profiles. In all the above cases, the corresponding rectangular pulses of the same RF amplitude failed to meet the required bandwidth coverage and had a poor tolerance to B_1 inhomogeneity. We also observed that reducing pulse lengths to below 480 μs for the UR-90° pulses and to below 540 μs for the UR-180° pulses demanded relaxed constrains that are a smaller B_1 inhomogeneity or a higher RF amplitude, both of which are undesirable.

The above-reported efficacies for the UR pulses compared to the rectangular pulses can be understood from the simulation movies (movies S1 and S2) of spins on the Bloch sphere generated by solving the Liouville–von Neumann equation for their dynamics under the influence of our UR pulses and for comparison with corresponding hard pulses of the same power. In movie S1, the effect of a UR-180° pulse is compared with that of the hard-180° pulse with the same RF amplitude, and in movie S2, an analogous comparison is done for a UR-90° and hard-90° pulse of the same RF amplitude. By focusing on the initial and final state for 11 spins within an offset range of ±7.5 kHz and three different B_1 fields (i.e., miscalibrated by −10, 0, and +10%), we see that both UR-180° and UR-90° pulses perform robust 90° or 180° unitary rotations, which is impossible using the rectangular pulses of the same RF amplitude. It is worth appreciating the intricate excursions on the Bloch sphere taken by different spins under the influence of the UR pulses to compensate for the range of offsets and B_1 inhomogeneity effects, which are unlike the intuitive rotations carried out under the influence of hard or rectangular pulses.

We also observe a mirror symmetry about the midpoint of the pulse phases for two of the UR-^{15}N pulses shown in fig. S2 (D and F). Such a symmetry was absent in all our ^{1}H pulses; thus, we consider it a curiosity potentially worth exploring in future work. In general, we observe two types of symmetry for our UR-90° and UR-180° pulses; these are described as type I and type IV previously (*43*). The pulses with type I have a mirror symmetry in the middle for both the x and y control components of the pulse shape when represented in the Cartesian coordinates. In the case of type IV, both the x and y control components have antisymmetric profiles (*43*). As a representative example, a UR-180°-^{15}N pulse with such a mirror (type I) symmetry is shown in fig. S9A. We also observe the expected correlation between the spin trajectory and the mirror symmetry of such UR pulses. This relation is presented in fig. S9 (B to D) where the purple curve shows the trajectories during different transformations possible using the UR-180° pulse shown in fig. S9A. The yellow curves are the time-reversed trajectories after flipping the purple curve to illustrate the symmetry relation about the midpoint of the pulse. As observed from these plots, a mirror symmetric UR-180°-^{15}N pulse produces trajectories with two types of symmetries. The spins starting along the unitary rotation axis (x axis for the above pulse) preserve mirror symmetry under both offset and B_1 inhomogeneity variations. In the case of

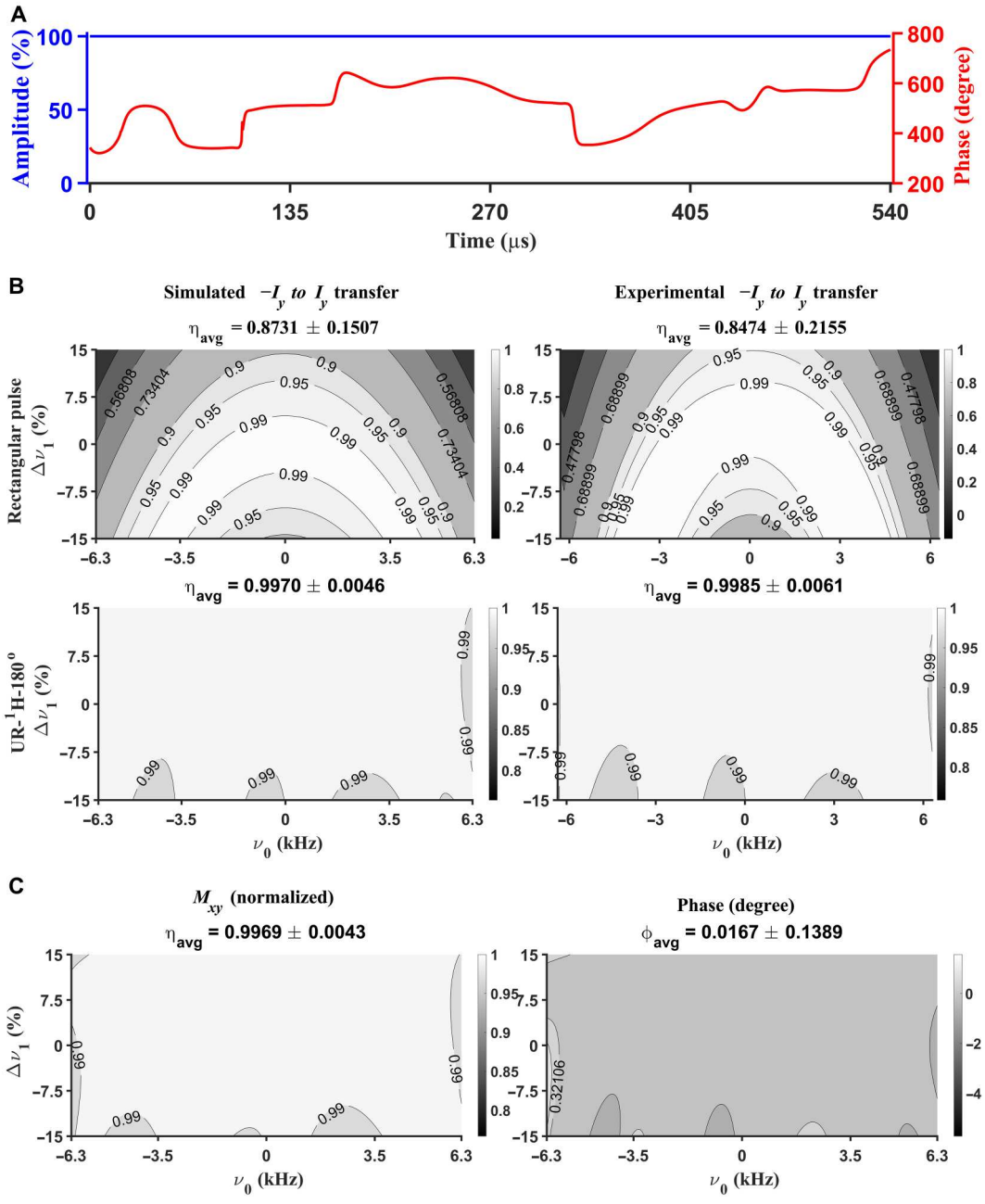

Fig. 1. Simulated and experimental performance of a low-power UR-180° pulse. (**A**) Example of the low-power UR-180° pulse with a duration of 540 μs, RF amplitude of 7.5 kHz, bandwidth of ±6.3 kHz, and B_1 inhomogeneity compensation of ±15%. (**B**) The simulated and experimental 2D excitation profiles obtained for the above pulse are represented as a contour plot (bottom panels) along with the 2D excitation profiles of a rectangular pulse of the same RF amplitude in the top panel. In these plots, offset (ν_0) in kilohertz is shown along the abscissa, and the deviation from the real RF amplitude ($\Delta\nu_1$) in percentage is shown on the ordinate. The average performance index is given on top of each panel as η_{avg} for the $-I_y$ to I_y transfer of these pulses. The region with transfer efficacy greater than 0.99 is represented in the lighter shade inside the first inner contour in all the plots. (**C**) The transverse magnetization retained after the UR-180° pulse is shown in the first panel. The average normalized transverse magnetization, $|\mathbf{M_{xy}}|$, within the region of interest is given at the top of the first panel. The phase error obtained after the UR-180° pulse is shown in the second panel, and the average phase error is given as ϕ_{avg} on top of this panel in degrees.

spins that are being inverted (I_z to $-I_z$) or refocused (I_y to $-I_y$), we observe an inversion symmetry (reflection about the midpoint followed by a sign change) about the midpoint under both offset and B_1 inhomogeneity variations. Such symmetric trajectories are absent for the spins under the action of the UR-180° pulse shapes for which a mirror symmetry was absent. The above symmetry relations can be observed in movie S3 where the top panel shows the effect of the UR-180° pulse (fig. S2E) without any mirror symmetry and the bottom panel for a UR-180° pulse (fig. S2F) with the mirror symmetry. In the case of the UR-90° pulse (fig. S2D) with a mirror symmetry, only for the trajectories of spins starting along the unitary rotation axis, we observe a conserved symmetry. To the best of our knowledge, so far it has not been proven that symmetric shaped pulse solutions are the global optimum for a GRAPE optimization. In practice, one gets completely dissimilar solutions without significant statistical correlation between the shapes if different initial starting points are chosen for the GRAPE optimization (*72*). From our UR-180° and UR-90° pulses, we observe a complete symmetry breaking for all the pulse shapes that had a smaller RF amplitude to bandwidth ratio. We also notice that having a larger ratio is not the only necessary requirement for obtaining pulse shapes with a mirror symmetry. As seen from the experimental excitation profiles discussed in the above sections for all our UR pulses, we do not observe any noteworthy correlation between the performance and the mirror symmetry of a pulse. Hence, understanding the role of symmetry, if any, in the GRAPE pulse shapes remains an open problem at the time this study was conducted.

Performance of low-power 2D-[^{1}H,^{15}N]-HSQCs and 2D-[^{1}H,^{15}N]-TROSY at 1.2 GHz

As observed from the simulated and experimental 2D excitation profiles of the UR-180° and the UR-90° pulses, they act as an ideal pulse with a minor phase error ($\phi_{avg} < \pm 0.25$ degree) inside the optimized range of offsets and B_1 values. Thus, we expected that these pulses could be used as direct replacement elements for all the hard pulses in any existing standard biomolecular NMR experiment. We tested this by modifying the commonly used 2D-[^{1}H,^{15}N]-HSQC experiment. For brevity, we will refer to this sequence as HSQC in the following discussions. The HSQC experiment provides a fingerprint spectrum with a 2D correlation between the chemical shift of a covalently bound proton and a nitrogen atom from each amino acid in a protein. Such a correlation spectrum is characteristic of a specific protein state and hence is a common starting point for protein NMR studies. For all the OC sequences constructed in this study, we make a comparison with corresponding high-power (with RF amplitudes of 35.57 kHz on the ^{1}H channel and 6.41 kHz on the ^{15}N channel) standard sequence and a low-power (with RF amplitudes of 8 kHz on ^{1}H channel and 5 kHz on ^{15}N channel) standard sequence. The low-power versions of the standard experiments are used in this study as an approximate experimental simulation of the worst-case scenario on a 5-mm inverse cryoprobe when a sample with high salt concentration is used. The OC pulse sequence for the HSQC experiment is shown in fig. S10A. When we tested the OC-HSQC at 1.2 GHz equipped with a 3-mm cryoprobe, we observed an improvement of 2.7% in the mean S/N ratio compared to the high-power standard sequence (figs. S11 to S13) for our test sample containing ubiquitin protein in a phosphate buffer. The improvement can be appreciated from the overlay of HSQC spectra obtained with the standard sequence and the OC sequence in fig. S11. The S/N improvements observed for various amide (NH) backbone peaks can be seen in the traces along the ^{1}H dimension in fig. S12. These enhancements are quantified in fig. S13 where the average improvement is shown as a dotted line. We observed an improvement of up to 277% in the mean S/N ratio (fig. S13) compared to the low-power version of the standard HSQC experiment. We attribute the improvements from the OC sequence to the better compensation for offset and B_1 inhomogeneity by the UR shapes. To test whether such a robust compensation by the pulses would give better enhancements for the sequences with more pulses, we constructed OC versions of 2D-[^{1}H,^{15}N]-HSQCSI (heteronuclear single quantum correlation with sensitivity improvement, for brevity referred to as HSQCSI) and 2D-[^{1}H,^{15}N]-TROSY (for brevity referred to as TROSY). The version of HSQCSI we are using has four additional pulses, and TROSY has two additional pulses on the ^{1}H channel. Both of these experiments provide the same information as HSQC, but in addition, HSQCSI delivers sensitivity enhancement for moderately sized proteins (*3*) and TROSY is essential for studying large proteins with considerable transverse relaxation (*3*). As an example, the pulse sequence for the low-power OC-TROSY is shown in Fig. 2A. The comparison of its performance at 1.2 GHz to the high-power standard TROSY and with the low-power standard TROSY (same RF amplitude as for the OC-TROSY sequence) is shown in Fig. 2B and fig. S14 as an overlay. It is visually evident from the projections shown in Fig. 2B that low-power OC-TROSY outperforms the standard sequence that uses hard pulses. The above improvements are better observed from the traces shown along the ^{1}H dimension for a set of selected NH peaks in Fig. 3A and for all the observed backbone NH peaks in fig. S15. These enhancements are quantified in Fig. 3B as a normalized S/N ratio for all the peaks along with normalized mean values. The mean values and coefficients of variation for different peaks within the same spectrum are tabulated in table S1 for all the above 2D experiments. On average, we see an improvement of 26% in the S/N ratio for OC-TROSY compared to the high-power standard sequence. The improvements are even more marked if we compare them to the low-power implementation of the standard TROSY sequence, where we see an improvement of 416% in the mean S/N ratio (Fig. 3B). The pulse sequence for OC-HSQCSI is given in fig. S9B. When we used this modified sequence at 1.2 GHz, we observed an improvement of 20% in the mean S/N ratio compared to the high-power standard HSQCSI and an enhancement of 590% in the mean S/N ratio compared to the low-power standard HSQCSI (figs. S16 to S18). The above enhancements were in agreement with our expectation, suggesting that compensating for the offset effects and B_1 inhomogeneity can provide improvements for longer bio-NMR sequences at 1.2 GHz. Furthermore, the successful implementation of these sequences shows that the low-power UR-180° and the UR-90° pulses are suitable for direct replacement of the hard pulses and thus can be used for constructing any low-power bio-NMR experiment. The marked improvements of up to 26% compared to a high-power sequence are obtained using OC pulses that had approximately 20 times lower power on ^{1}H and 1.6 times lower power on ^{15}N for a 3-mm inverse cryoprobe at 1.2 GHz.

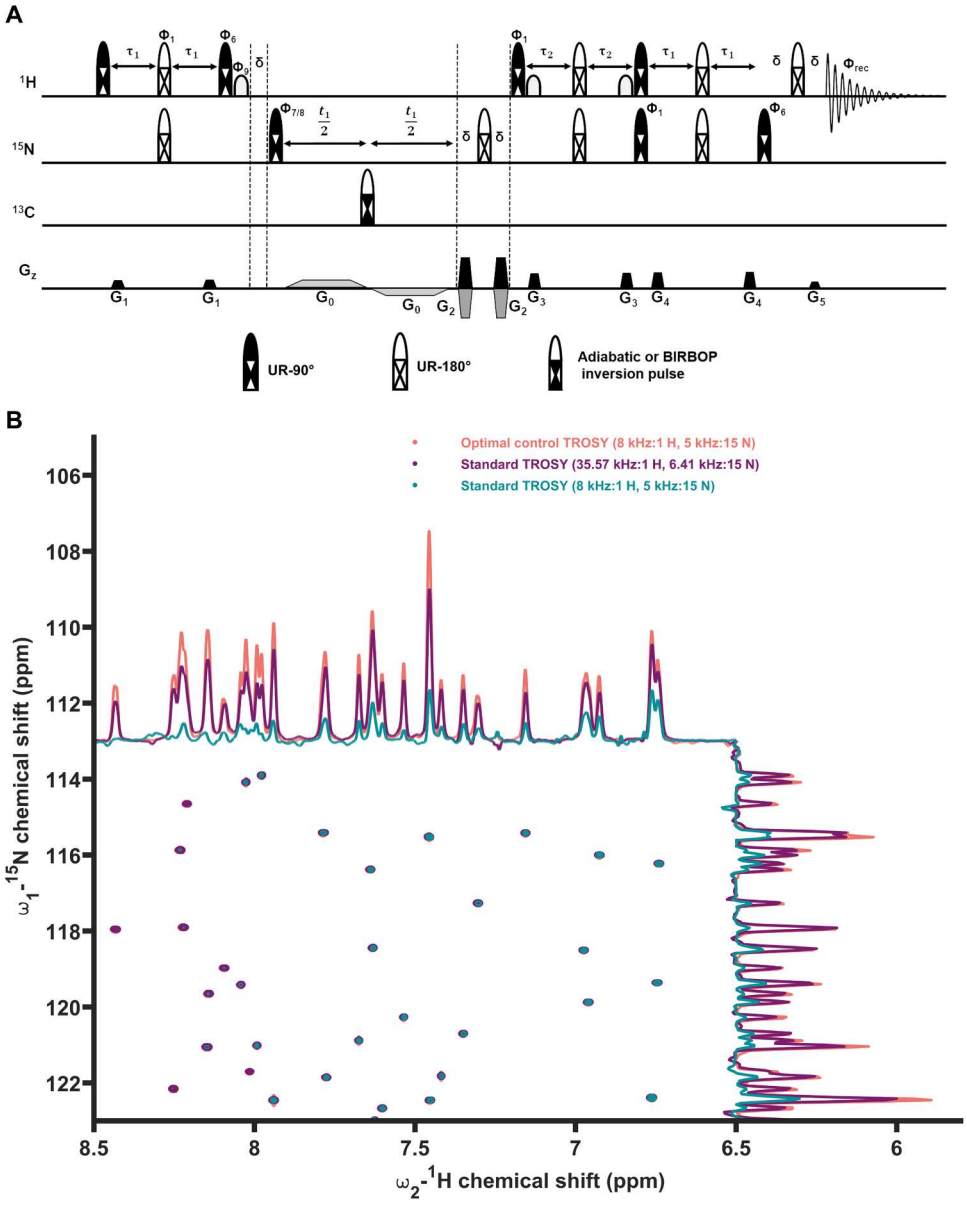

Fig. 2. Low-power 2D-OC-[^{1}H,^{15}N]-TROSY experiment. (**A**) Schematic representation of the 2D-OC-[^{1}H,^{15}N]-TROSY pulse sequence (further details are given in the Supplementary Materials). (**B**) Selected region from the spectra overlay of 2D-OC-[^{1}H,^{15}N]-TROSY (rose color spectra) and its standard version with maximum RF amplitude possible for the hard pulses (magenta color spectra) on a 3-mm inverse cryoprobe at 1.2 GHz. The corresponding low RF amplitude version (cyan color spectra) for simulating the power-limited situation on a 5-mm inverse cryoprobe at 1.2 GHz.

Multiband selection using a single OC pulse with multinutation angles for differential control of the ^{13}C spins in proteins

Initially, we tried to optimize for shapes obeying the scheme in fig. S1C using the GRAPE procedure, but we were unable to generate shapes that were shorter than 380 μs when our low-power criteria are used. Hence, we decided to use the multiband-selective scheme that is popular in Hadamard NMR experiments (*66*, *73*). In this context, we use the well-known distribution of chemical shift ranges of the ^{13}C spins in proteins [fig. S19 based on distributions from Biological Magnetic Resonance Data Bank (BMRB) database]. Such an approach for two-band control has been used earlier for designing OC pulses without Bloch-Siegert shifts (*54*). In our scheme, we aim to control two chemical shift ranges simultaneously with two different nutation angles for the spins in these two regions. There have been previous studies on optimizing multiband-selective (*54*, *64*) pulses using OC theory, but to the best of our knowledge, there are no studies with multiple nutation angles in a single pulse for different bands. A common fidelity (*64*) used for such multiband-selected GRAPE optimization procedure to achieve a PP transformation in B number of bands is

$$\Phi_{\mathrm{pp}}^{(\gamma)} = \sum_{b=1}^{B} \Phi_b \tag{2}$$

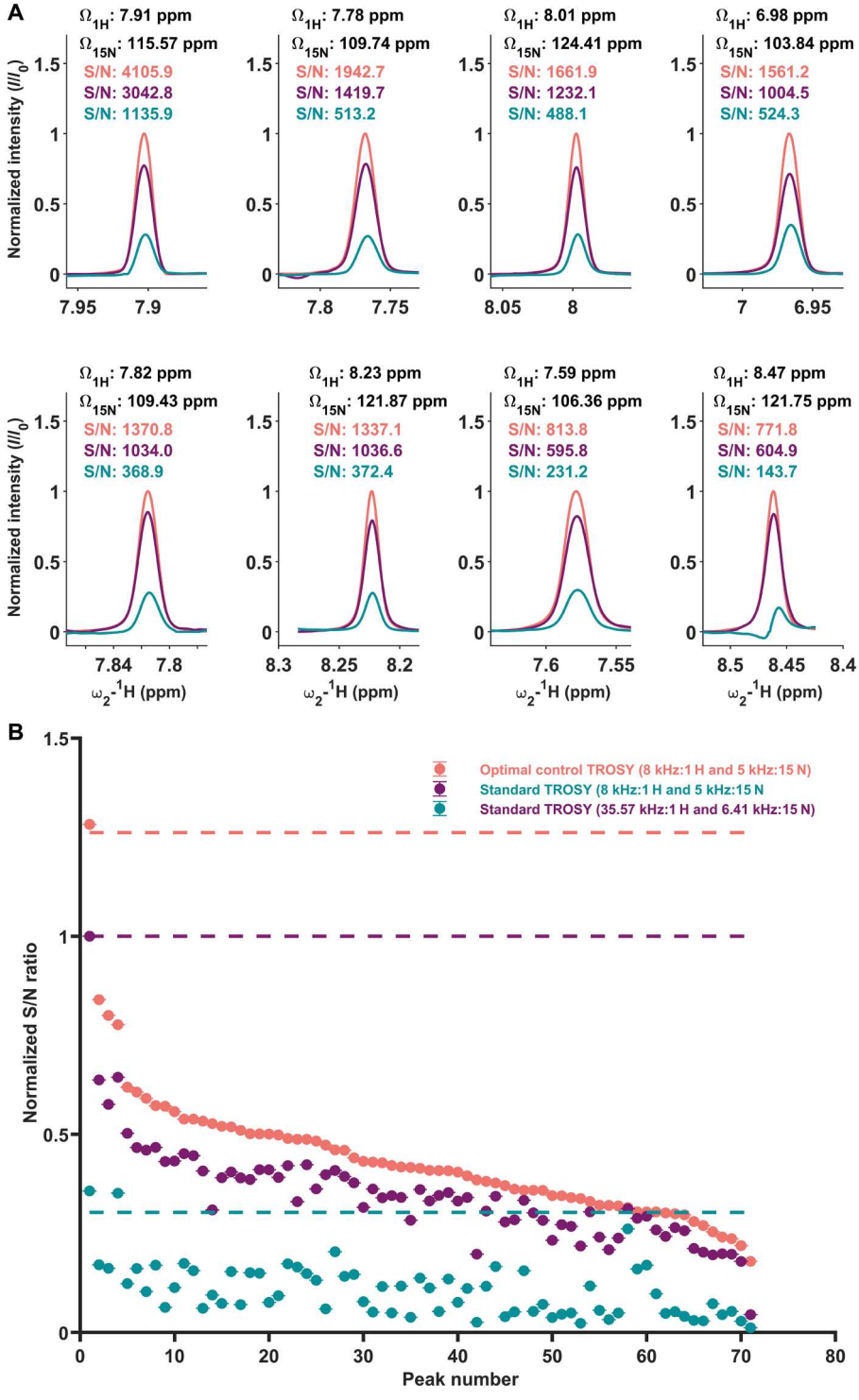

Fig. 3. The enhancement in S/N ratio observed with the 2D-OC-[^{1}H,^{15}N]-TROSY at 1.2 GHz. (**A**) Overlay of a selected set of traces through backbone NH peaks that are observed in the TROSY spectra from fig. S10 with the same color coding. The peak position in parts per million and the S/N for each trace are given in respective color on top of each subpanel. (**B**) The normalized S/N ratio for different backbone NH peaks from the above TROSY spectra is shown for comparison. The peak numbers shown on the abscissa are in descending order of the S/N ratio from the OC-TROSY spectrum. The average values from each spectrum are shown as a dotted line in their respective color.

where γ can be *x*, *y*, or z depending on the initial operator state that is controlled in the PP transformation. The ensemble-averaged fidelity for the *b*th band with *N* offsets in the system Hamiltonian, $\hat{H}^{(0)}$, and *M* different B_1 fields in the controls is calculated as

$$\Phi_b = \frac{\sum_{n=1}^{N}\sum_{m=1}^{M}\Phi[c^{(k)}(t)]}{(N \times M)} \quad (3)$$

$\Phi[c^{(k)}(t)]$ is given by Eq. 1. We can generate UR pulses by averaging over the three possible $\Phi_{pp}^{(\gamma)}$ fidelities

$$\Phi_{UR} = \frac{1}{3}\sum_{\gamma}\Phi_{pp}^{(\gamma)} \quad (4)$$

This approach of combining different fidelities for each band would be expensive if we need to introduce multiple nutation angles additionally. As an alternative approach, we notice that the fidelity function $\Phi_{pp}^{(\gamma)}$ given as a summation of Φ_b in Eq. 2 can be equivalently reformulated as

$$\Phi_{pp}^{(\gamma)} = \Phi_b \quad (5)$$

if we redefine our system Hamiltonian $\hat{H}^{(0)}$ as

$$\hat{H}^{(0)} = \sum_{b=1}^{B}\hat{H}^{(0,b)} \quad (6)$$

and the desired target state after a rotation through an arbitrary angle θ_b in the *b*th band as

$$\sigma_{tar} = \sum_{b=1}^{B}\sigma_{tar}^{(b)}(\theta_b) \quad (7)$$

Such a definition would also allow combining the UR and PP targets without introducing a summed fidelity function with the additional computational cost (*57*) proportional to the number of bands from evaluating *B* term in the summation in Eq. 2. We were able to implement this procedure without any modification of the default fidelity calculation in the OC module of Spinach software. This procedure can thus easily generate any finite number of different nutation angles for the same number of bands using a single pulse.

We illustrate this concept by constructing three types of band-selective pulses; the first example is a set of eight pulses for protein NMR experiments. The second and third examples are to demonstrate the generality of this approach. First, we generate pulses that control two chemical shift ranges simultaneously with two different nutation angles. The example pulse shape shown in Fig. 4A is a band-selective pulse that can selectively rotate C_α spins through a UR-180° rotation without in effect disturbing the CO spins through a UR-360° rotation. As seen in Fig. 4A, this shaped pulse achieves two-band excitation: For the first band with the C_α spins represented in orange color, the pulse acts as a UR-180° pulse, and for the second band with the CO spins in green color, it acts as a UR-360° pulse. On the basis of the above results, we use a modified scheme for designing low-power band-selective pulses for the protein NMR experiments. This modified scheme is shown in Fig. 4B, where we have three regions, which are a controlled active region that does a UR or PP-90° rotation or a UR or PP-180° rotation, and a controlled inactive region that does a UR-360° rotation or equivalently an effective 0° rotation. We leave the rest of the region as uncontrolled, thus considerably reducing the RF amplitude requirements of this OC scheme. Using the above scheme, we designed pulses for the CO or the C_α UR-90° or UR-180° transformations without perturbing the C_α or CO spins, respectively, and pulses for the CO or the C_{ali} UR-90° or UR-180° transformations without perturbing the C_{ali} or CO spins, respectively. The pulse that affects UR-180° on the C_α spins without perturbing the CO spins is named band-selective C_α 180° universal rotation (CO preserved) by optimized pulse, abbreviated to BSCa(CO)URBOP-180°. The simulated and experimental excitation profile of the above pulse is shown in Fig. 4C for the I_z to $-I_z$ transformation of this pulse. We can see the robustness of the OC pulse to the offset and B_1 field variation within the controlled active and inactive regions from these profiles. The set of final pulse shapes designed to differentially control the CO and C_α spins is shown in fig. S20. Initially, we designed pulse shapes with an RF amplitude of 15 kHz and B_1 inhomogeneity compensation of ±20%. The pulses that did a UR-90° rotation in the controlled active region had a duration of 290 μs, and those that did a UR-180° rotation in the controlled active region had a duration of 300 μs. We obtained pulse shapes that can be used for samples with higher salt concentrations by further ramping down the RF amplitude to 12 kHz and relaxing B_1 inhomogeneity compensation to ±15%. The reduction in the B_1 inhomogeneity compensation to ±15% was necessary to limit pulse duration to 380 μs. In these pulse shapes, those that did a UR-90° rotation in the controlled active region had a duration of 360 μs, and those that did a UR-180° rotation in the controlled active region had a duration of 380 μs. All the above shapes had transfer efficacies greater than 0.99 (in most cases, it was $\eta_{avg} > 0.995$ with a few exceptions) for the necessary operator transformations in both the controlled regions. This can be seen from the simulated and experimental 2D excitation profiles shown in figs. S21 to S26. The above shapes retained greater than 99.5% of the net transverse magnetization for the controlled active region and above 99% for the controlled inactive regions. They also show a small phase error with ϕ_{avg} less than ±0.25° in the simulations. The efficacy of this category of band-selective pulses can be appreciated from the spin dynamics in movie S4 showing the simulation of such a two-band differential control using BSCa(CO)URBOP-180° and BSCa(CO)URBOP-90° pulses by solving the Liouville–von Neumann equation. In both the simulations, C_α spins in orange color do either a UR-180° or UR-90° rotation under the influence of the respective pulse shapes with robust efficacy. A clear difference between the stop band in the Gaussian cascade band-selective pulses and our controlled inactive region is that we permit the freedom to move around the Bloch sphere for all the spins during the low-power pulses.

More demanding circumstances are encountered when both C_{ali} and CO spins need to be controlled differently using a single pulse. The requirement of controlling a bandwidth of at least 24 kHz (80 ppm) for the C_{ali} region exerts higher RF amplitude demands for the shaped pulses. A recent study to design such selective universal rotations by optimized pulses (SURBOP) for C_{ali} selection involved quaternions to represent universal rotation (*57*). As seen from fig. S27, the SURBOP-180° and SURBOP-90° shapes have a good experimental performance within the 24-kHz bandwidth for which they are optimized to work. The experimental efficacy for the SURBOP-

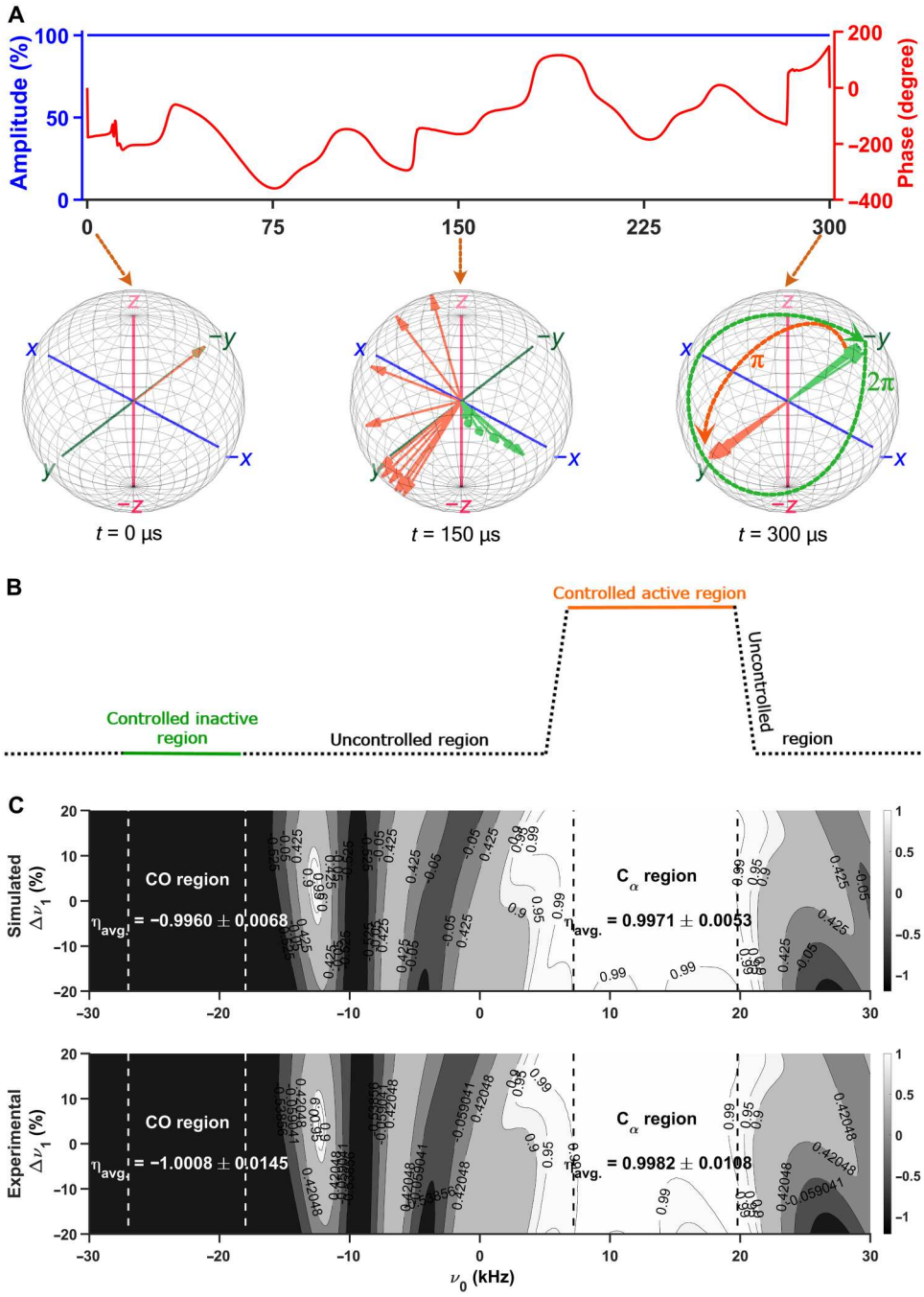

Fig. 4. Low-power OC band-selective pulse. (**A**) An example of the two-band–selective pulse, with an RF amplitude of 15 kHz, a pulse duration of 300 µs, and B_1 inhomogeneity compensation of ±20%. The effect of this pulse is shown for spins in two selected bands. The spins that are experiencing a UR-180° rotation in the first band are shown in the orange color, and the spins in the second band undergoing a UR-360° rotation are in the green color. The effect of the pulse is shown at three time points, with all spins starting from the $-y$ direction at time $t = 0$. The dotted arrows shown on the Bloch sphere at $t = 300$ µs with the angles in radians marked with their respective colors are to indicate the net rotation for the spins in each band, and this does not represent the path taken by the spins under the OC pulse. (**B**) The modified scheme for designing the two-band–selective pulses has three regions, which are controlled active (in orange color), controlled inactive (in green color), and uncontrolled (in black color) regions, respectively. (**C**) The simulated and experimental 2D excitation profiles obtained for the I_z to $-I_z$ transfer of the BSCa(CO)URBOP-180° pulse following the scheme in (B) are shown as contour plots. In these plots, offset in kHz ($\Delta\nu_1$) is given along the abscissa, and the deviation from the real RF amplitude ($\Delta\nu_1$) in percentage is shown on the ordinate. The average performance index is represented by η_{avg} for the respective transformation using the pulse. The region represented in a lighter shade that is inside the first inner contour is for contour values greater than 0.99 in the controlled active region.

90° shape is η_{avg} of 0.9598, and that for the SURBOP-180° shape is η_{avg} of 0.9917. The major limitation of the SURBOP shapes is their lower tolerance to B_1 inhomogeneity of ±5%. In our experience, at 1.2 GHz, a B_1 inhomogeneity compensation of at least ±15% is necessary to robustly reproduce the performance of the pulse shapes. A smaller B_1 inhomogeneity compensation will result in a substantial deviation from the simulated excitation profiles during the experiment. We investigated whether the modified two-band–selective scheme could reduce the power demands or alternatively reduce the pulse duration for a given RF amplitude. To our delight, equivalent shaped pulses could be generated with shorter duration using the modified two-band–selective scheme. The decrease in pulse duration can be understood from the excitation profiles generated by the SURBOP pulses and the Gaussian cascade pulses. We notice that the region outside the large stopbands (42 kHz each) of the SURBOP pulses (*57*) behaves similarly to our uncontrolled region, whereas in the Gaussian cascade pulses stopbands extend to infinity without actively controlling the spins. This difference shows that the two large stopbands flanking the transition band in the SURBOP pulses consume part of the RF power to control the spins to achieve minimal perturbation from their initial state. This is unlike our small controlled inactive region where spins have the freedom to move around the surface of the Bloch sphere before returning to the initial state, hence reducing the RF power demands. The set of pulse shapes we generated is shown in fig. S28 (C, D, G, and H). In the reported pulses, those that did a UR-90° rotation in the controlled active region had a duration of 265 μs and those that did a UR-180° rotation in the controlled active region had a duration of 270 μs, with an RF amplitude of 15 kHz and B_1 inhomogeneity compensation of ±5%. We observe approximately 20% reduction in the pulse duration with the two-band–selective scheme shown in Fig. 4B. The ability to compensate for stricter set of constrains by different excitation schemes can be understood from the ratio of bandwidth to pulse duration given in fig. S29 for the corresponding shaped pulses with the same RF amplitude. We observe that a shorter pulse length for a given RF amplitude or alternatively a lower RF amplitude for a given length is possible by careful choice of the excitation scheme that is used for generating OC band-selective pulses. As seen from the simulated 2D excitation profiles in figs. S30 and S31, all our band-selective shapes had acceptable transfer efficacies for the operator transformations in the controlled active and inactive regions. The experimental 2D excitation profiles (fig. S32) were comparable to those obtained for the SURBOP pulses. Because larger B_1 inhomogeneity compensation is necessary for a robust experimental performance, we increased the compensation range to ±15% for the above shapes and obtained pulses shown in fig. S28 (A, B, E, and F). This resulted in shapes with a duration of 330 μs for pulses that did a UR-90° rotation in the controlled active region and a duration of 350 μs for the shapes that warranted a UR-180° rotation in the controlled active region. All the final shapes had an RF amplitude of 15 kHz and covered a bandwidth of 24.6 kHz in the C_{ali} region and 9 kHz in the CO region. As observed from the simulated and experimental 2D excitation profiles in figs. S33 to S35, we see an improvement in transfer efficacies after including a larger B_1 inhomogeneity compensation and have an acceptable phase error ϕ_{avg} of less than ±0.30°. We also developed pulses with B_1 inhomogeneity compensation of ±20%, but this resulted in even longer pulse durations, which were greater than 380 μs, and hence are not used in this work.

A summary of the performance obtained with the low-power OC band-selective pulses developed for the 3D-solution NMR experiments of the protein samples is presented in Fig. 5. In total, we designed eight types of two-band differential control pulses for the CO and C_α spins or the CO and C_{ali} spins with the controlled active region realizing either a UR-180° or UR-90° rotation. The experimental robustness of the final pulse shapes we designed becomes obvious from a simple 1D-^{13}C experiment using the above OC band-selective pulses as seen in the results shown in Fig. 5. The two-band differential control that these pulses execute is clear from a comparison with the normal carbon 1D spectra obtained with a hard pulse.

We now illustrate the generality of our multiband scheme with different nutation angles per band by constructing the following examples. A single-band–selective pulse for UR(180°, 90°) rotation combinations is designed to show how two arbitrary nutation angles can be carried out at two different bands using a single pulse. The shape obtained for such a UR(180°, 90°) pulse is shown in Fig. 6A. In this example, two different bands are controlled using the above pulse: In the first band, spins in green color undergo a UR-180° rotation, and in the second band, spins in orange color undergo a UR-90° rotation. The last example demonstrates how PP and UR rotations can be combined in a single pulse along with the three-band selection. The UR(180°)-UR(360°)-PP(90°) pulse shown in Fig. 6B does a UR-180° rotation in the first band, a UR-360° rotation in the second band, and a PP-90° rotation in the third band. This can be observed from the excitation profiles shown in Fig. 6 (C to E). The influence of the UR(180°)-UR(360°)-PP(90°) pulse on I_z magnetization is shown in Fig. 6C, on I_x magnetization is shown in Fig. 6D, and on I_y magnetization is shown in Fig. 6E. We observe that the pulse executes a three-band selection with different nutation angles in each band. In the above examples, we have demonstrated that two-band and three-band selection can be combined with different nutation angles with the UR and/or PP combinations in these bands using a single pulse. This procedure can be easily extended to a larger number of bands ($B > 3$) and nutation angles other than 90°, 180°, and 360°. Further studies are needed to completely explore the scopes and limits of this category of OC pulses.

Performance of the low-power 3D-HNCO and 3D-TROSY-HNCO experiments at 1.2 GHz

The set of OC band-selective pulses and the UR-^{1}H and UR-^{15}N pulses were used to construct low-power 3D bio-NMR experiments. In this work, we report the performance of low-power OC 3D-HNCO and 3D-TROSY-HNCO at the 1.2-GHz spectrometer equipped with a 3-mm inverse cryoprobe. We modified the existing standard Bruker pulse sequences to work with the low-power OC pulses. The pulse sequence diagrams for the 3D-OC-HNCO and 3D-OC-TROSY-HNCO experiments are shown in fig. S36. In the above 3D-OC experiments, either a water gate element or the flip-back pulses are used to achieve solvent suppression. The OC band-selective pulses on the ^{13}C dimension had an RF amplitude of either 15 or 12 kHz, and the ^{1}H and ^{15}N pulses had an RF amplitude of 8 and 5 kHz, respectively. As an example, the pulse sequence diagram for the low-power 3D-OC-HNCO is shown in Fig. 7A. The performance comparison between the high-power standard 3D-HNCO, the low-power standard 3D-HNCOs, and 3D-OC-HNCOs is shown in Fig. 7B and fig. S37 as an overlay of the 2D-[^{13}C,^{1}H]-

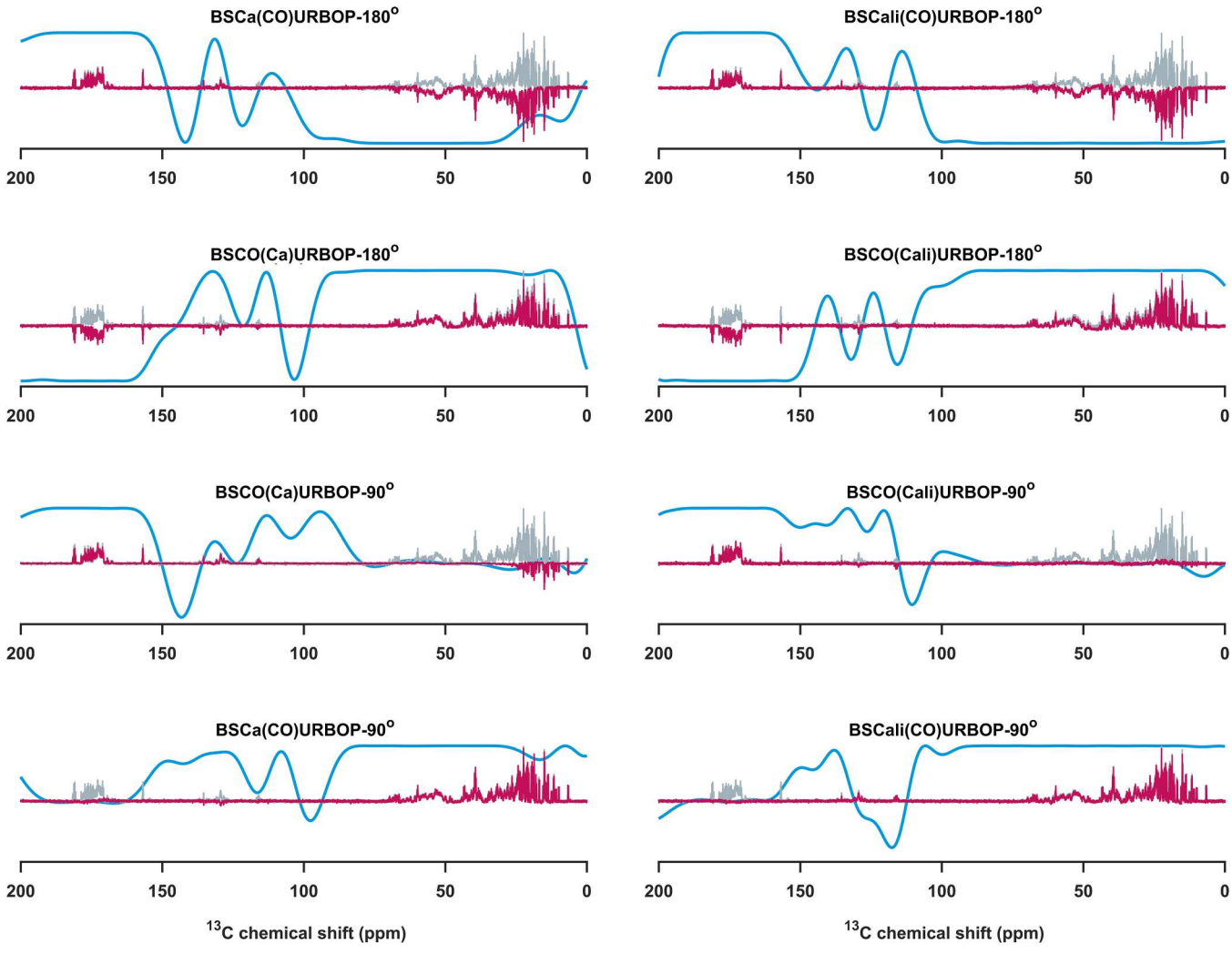

Fig. 5. A summary showing the effect of eight different OC band-selective pulses. The effect of eight different OC band-selective pulses developed in this work for achieving differential control of the ^{13}C spins in the protein samples. The results obtained using a labeled ubiquitin sample are shown as spectra in dark magenta color, and for comparison, a standard 1D ^{13}C spectrum is shown in gray color in all the panels. The expected excitation profile is shown as a blue curve in each panel. The abbreviated name of the corresponding pulses is given on top of individual panels.

projections. It is evident from these overlay plots and the projections along the ω_1 and ω_2 axes that the low-power OC-based sequence outperforms the standard 3D-HNCO sequence. A selected set of traces along the ^1H dimension showing these improvements is presented in Fig. 8A, and all the observed backbone NH-CO correlation peaks are in fig. S38. The careful inspection of the normalized S/N ratio for all the cross-peaks shows that the low-power 3D-OC-HNCO sequence has an average improvement in the S/N ratio of 17% (Fig. 8B) compared to the high-power standard 3D-HNCO with the maximum possible RF amplitudes on all the channels. The enhancement in the mean S/N is up to 270% (Fig. 8B) compared to the low-power implementations of the standard 3D-HNCO. We also observe an improvement in mean S/N ratio of 20% for 3D-OC-TROSY-HNCO when compared to the high-power standard 3D-TROSY-HNCO that had RF amplitudes much larger than possible for the hard pulses on a 5-mm inverse cryoprobe at 1.2 GHz. If we compare the 3D-OC-TROSY-HNCO experiment to the low-power implementation of the standard sequence, we see an enhancement of up to 411% in the mean S/N ratio (figs. S39 and S40). The traces along the ^1H dimension clearly showing these improvements are presented for all the observed backbone NH-CO correlation peaks in fig. S41. The average values and coefficient of variation for the peaks within different 3D-HNCO and 3D-TROSY-HNCO spectra are summarized in table S1. We also see a marginal improvement in the S/N ratio if the Gaussian cascade band-selective pulses with high RF amplitudes are replaced with our low-power OC-based band-selective pulses in the standard Bruker sequences at the high-field magnets from 800- to 1200-MHz spectrometers.

The extraordinary tolerance to B_1 miscalibration and the scope for automation

In this work, we generated and selected OC pulse shapes that compensated for a large B_1 inhomogeneity or miscalibration range of either ±15 or ±20%. Hence, these OC shapes can work as virtually calibration free pulses. In Fig. 9A, we show the tolerance upon

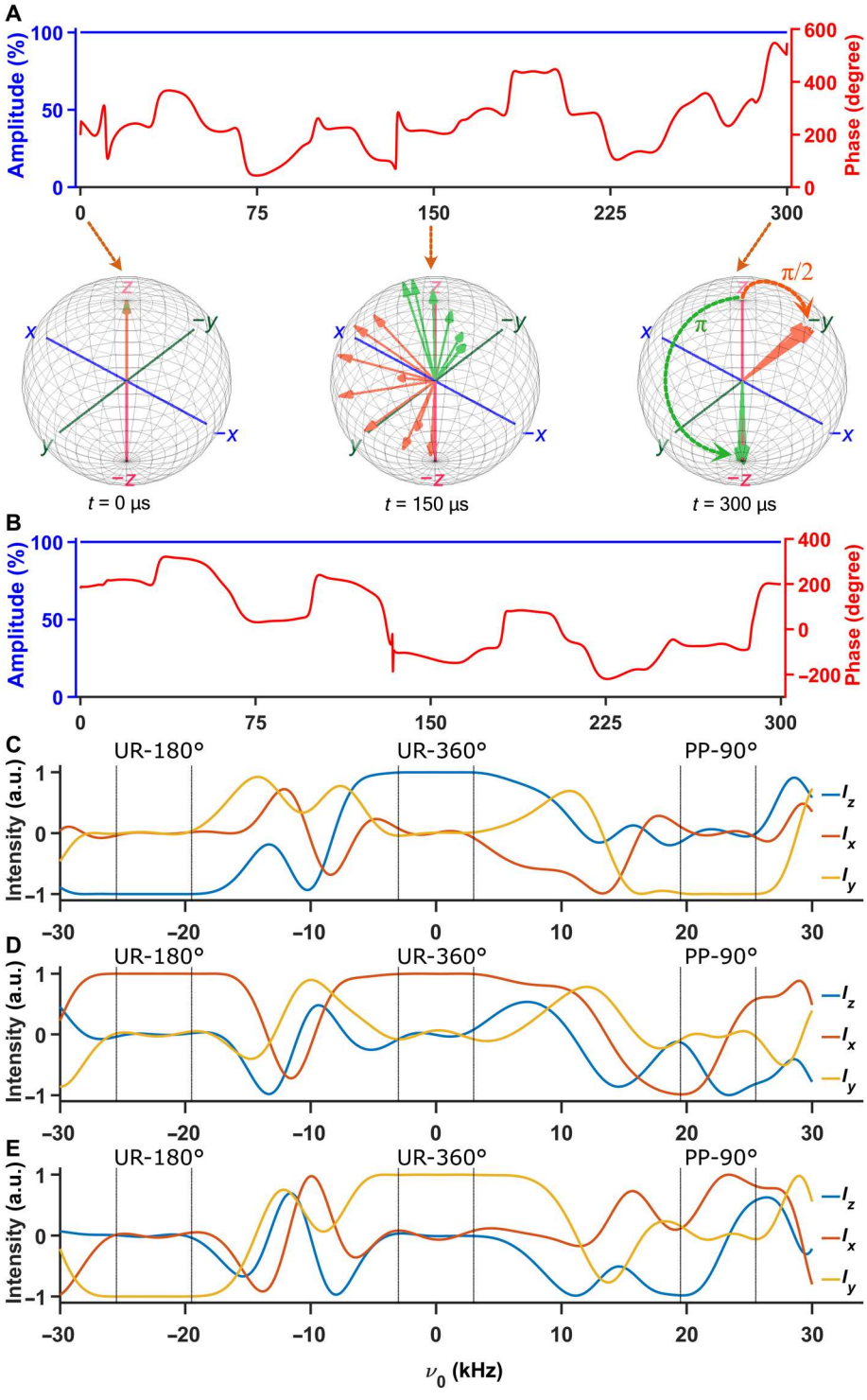

Fig. 6. Two- and three-band–selective OC pulses that produce different nutation angles in these bands with a single pulse. (**A**) Example for the UR(180°)-UR (90°) pulse with an RF amplitude of 15 kHz and a pulse duration of 300 µs. The effect of the above pulse is shown for spins in the two selected bands, spins that experience a UR-90° rotation in the first band are shown in orange, and the spins undergoing a UR-180° rotation in the second band are shown in green. The effect of the pulse is shown at three time points during the pulse; at time t = 0, the spins from both bands start along the z direction of the Bloch sphere. The dotted arrows shown in the Bloch sphere at t = 300 µs with the angles marked in radians are to indicate the net rotation for the spins in each band. (**B**) An example of a three-band–selective pulse shape that executes three different nutation angles of UR-180°, UR-360°, and PP-90° in these bands. The UR(180°)-UR(360°)-PP(90°) pulse had an RF amplitude of 15 kHz and a pulse duration of 300 µs covering 6 kHz in all the three bands. The excitation profiles obtained (**C**) for an initial I_z magnetization, in (**D**) for an initial I_x magnetization, and in (**E**) for an initial I_y magnetization. In all the profiles, the final I_z magnetization is in the blue profile, the I_x magnetization is in the orange profile, and the I_y magnetization is in the yellow profile. The three different bands are marked as separate regions on all the three panels. a.u., arbitrary units.

systematic miscalibration of all the three channels from −20 to +20% for the 3D-OC-HNCO experiment. The [^{1}H,^{13}C]-projection from 3D-OC-HNCO at the above miscalibrations is virtually indistinguishable with no observable phase or baseline errors. The variation due to these miscalibrations is quantified in Fig. 9 (B and C), and the average values are shown in fig. S42. We observe that the maximum variation in the mean S/N ratio and the average integrals is only −16% without any artifacts in the spectra. This variation is slightly less than the 17% improvement we see compared to a standard 3D-HNCO with the maximum achievable power on a 3-mm cryoprobe. Hence, even with large miscalibrations, we get performance that is in the worst case equal and otherwise with a smaller enhancement for the 3D-OC-HNCO experiment. We also observe a better tolerance for the positive B_1 miscalibrations than for the

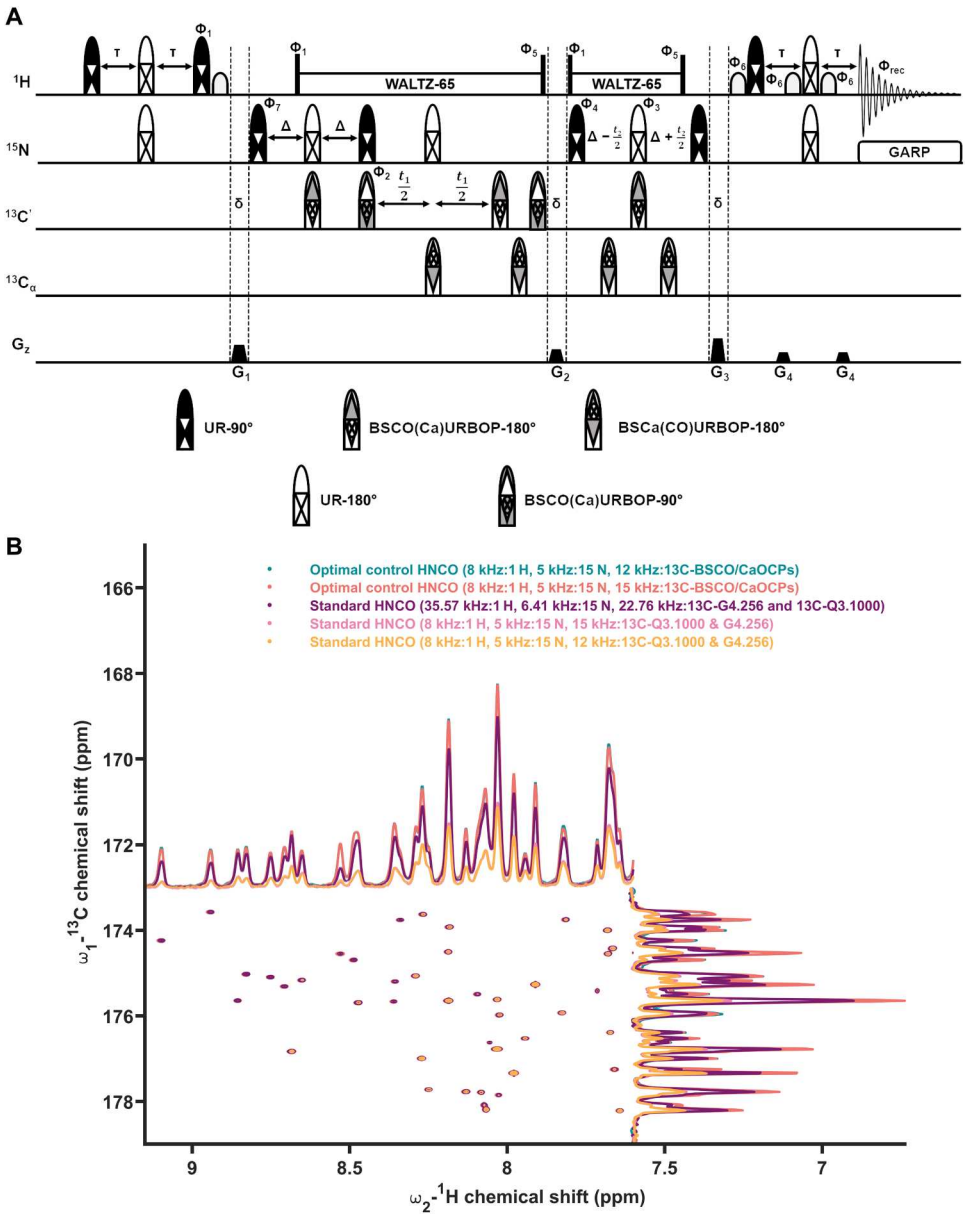

Fig. 7. Low-power OC 3D-OC-HNCO experiment. (**A**) Pulse program scheme of the low-power OC-based 3D-OC-HNCO (further details are given in the Supplementary Materials). (**B**) Selected region from the overlay of the standard 3D-HNCO (magenta color spectra) that had hard pulses with an RF amplitude of 35.57 kHz on the ^{1}H channel, 6.41 kHz on the ^{15}N channel, and 22.76 kHz for the Gaussian cascade pulses. 3D-OC-HNCO that had UR pulses with an RF amplitude of 8 kHz on the ^{1}H channel, 5 kHz on the ^{15}N channel, and 15 kHz (rose color spectra) or 12 kHz (cyan color spectra) for the band-selective OC pulses. The RF amplitude–limited situation on a 5-mm inverse cryoprobe at 1.2 GHz is simulated using the standard 3D-HNCO that had hard pulses with an RF amplitude of 8 kHz on the ^{1}H channel, 5 kHz on the ^{15}N channel, and 15 kHz (pink color spectra) or 12 kHz (yellow color spectra) for the Gaussian cascade pulses.

negative B_1 miscalibrations for the 3D-OC-HNCO experiment. This extraordinary tolerance is also observed in all the other OC sequences we discussed in this article (figs. S43 and S44 and table S2). The highest variation in mean S/N ratio was up to −22% for the 3D-OC-TROSY-HNCO experiment, and the mean integral was up to −25% for the 2D-OC-[^{1}H,^{15}N]-TROSY experiment. Hence, we expect that the low-power OC pulse sequences will help the researchers in automating the bio-NMR experiments without compromising the spectral quality at 1.2 GHz and conceivably at other high-field magnets starting from 800 MHz.

DISCUSSION

The recent availability of 1.2-GHz spectrometers is part of the continuing quest for higher-field magnets among the bio-NMR community. While these spectrometers provide unparalleled performance, they come with challenges because the broadband requirements of pulses demand power levels that are not tolerated by available probes, especially with large diameters such as a 5-mm cryoprobe. We demonstrated that robust low-power UR pulses can be designed for the ^{1}H and ^{15}N channels by careful optimization and evaluation of the pulse shapes. All the pulses we generated have

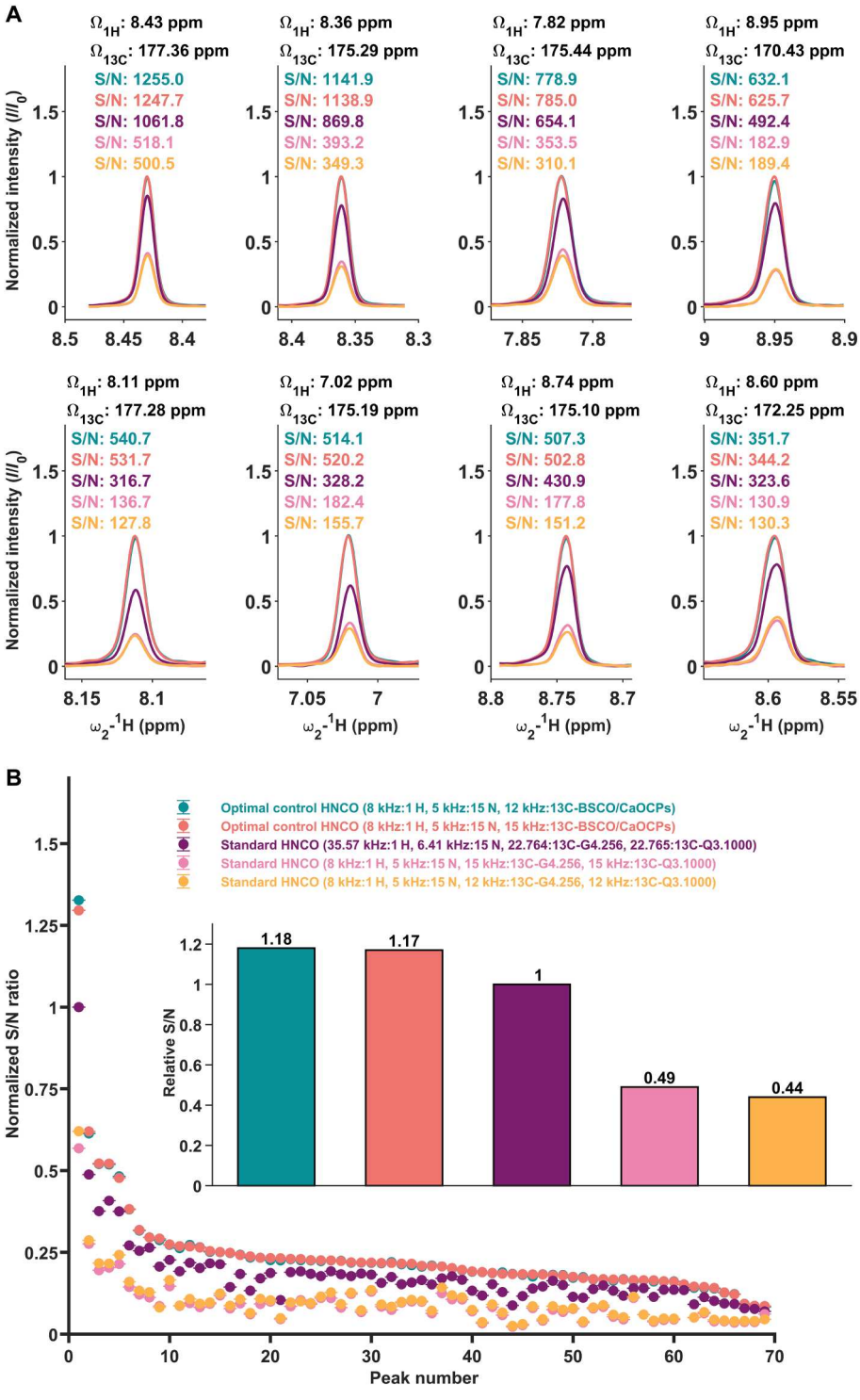

Fig. 8. The enhancement in S/N ratio observed with 3D-OC-HNCO experiment at 1.2 GHz. (**A**) Traces along the ^{1}H dimension showing the improvements observed for a selected set of backbone NH-CO correlation peaks from the spectra overlay in fig. S37 following the same color code. (**B**) The normalized S/N ratios for different backbone NH-CO correlation peaks and the mean values obtained for these experiments are shown as bar plots inside the panel. The peak numbers shown on the abscissa are in descending order of the S/N ratio from the 3D-OC-HNCO spectrum.

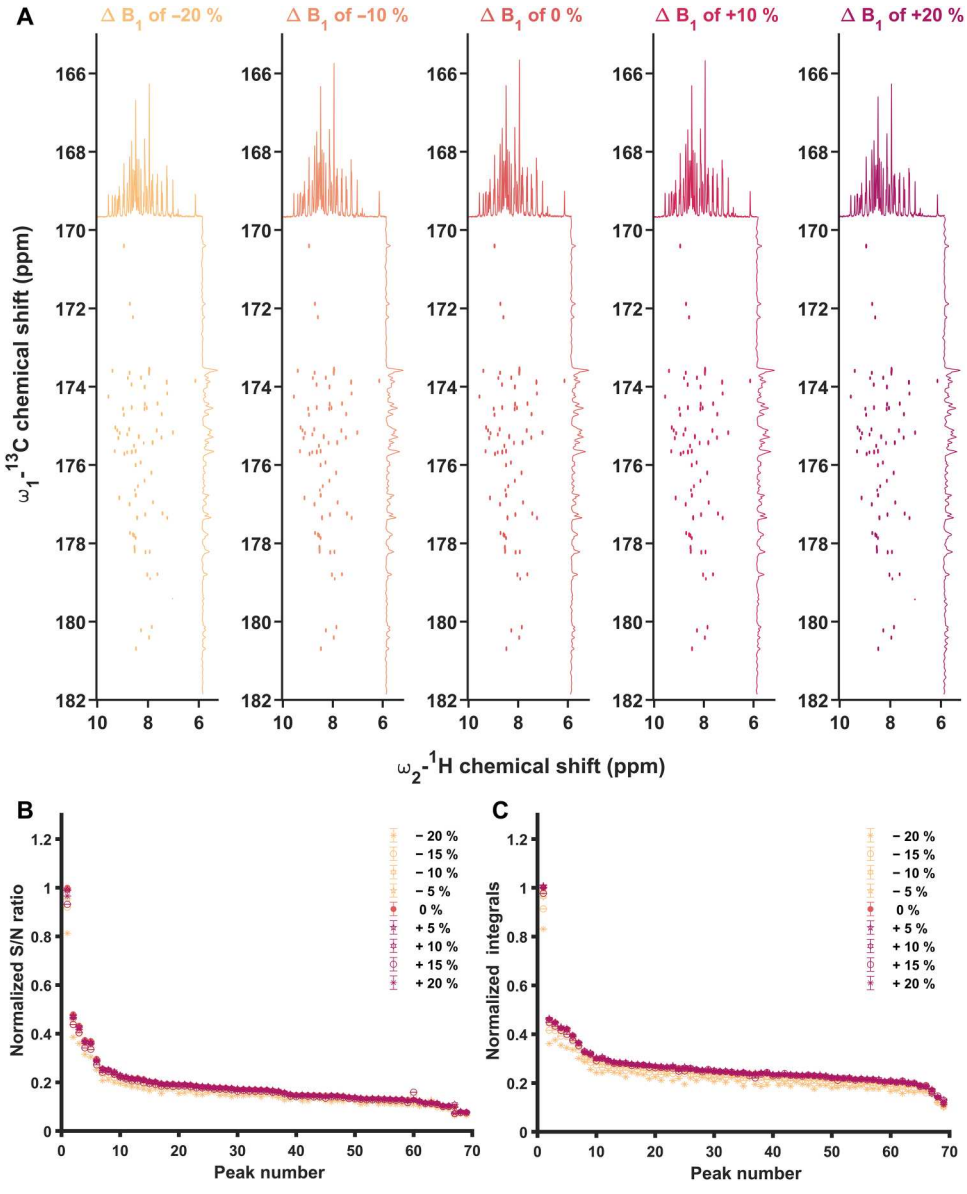

Fig. 9. The B_1 miscalibrated spectra obtained with the 3D-OC-HNCO experiment. The [^{13}C,^{1}H]-projection from 3D-OC-HNCO that was recorded by systematic miscalibration of all the three channels starting from −20 to +20% in systematic steps of +5%. (**A**) A selected set of such spectra at five such points are shown with the light orange color to the dark magenta color in the direction of increasing RF amplitude. (**B**) The normalized S/N ratios and (**C**) the normalized integral values from these miscalibrated spectra are shown for all the backbone NH-CO correlation peaks. The normalization was done with respect to the peak with the maximum value in the 3D-OC-HNCO spectrum that had 0% miscalibration.

generally smooth phase profiles and constant amplitude. They achieved the bandwidth demands of all the routine 2D-[^{1}H,^{15}N] correlation experiments such as HSQC, HSQCSI, and TROSY. In our experience, smoother pulse shapes were highly reproducible in contrast to the noisy-looking pulse shapes. These UR-180° and UR-90° pulse shapes were further selected on the basis of their performance in simulated and experimental 2D excitation profiles, where they exhibited an average performance index η_{avg} greater than 0.99 and had a minor phase error ϕ_{avg} less than ±0.25°. We also observe that there is no significant correlation between the symmetry of the pulse shape and its experimental performance. The above pulses were considered as a robust equivalent to ideal pulses, i.e., without any substantial offset effect, B_1 inhomogeneity effect, and phase errors within the optimized range. Hence, we demonstrate that they can be easily used as replacement elements for all the hard pulses in any bio-NMR sequences. The robustness of the UR pulses can be appreciated from the improvements in the mean integrals and the mean S/N ratios of the low-power OC pulse sequences (table S1). In all the 2D low-power OC sequences, we saw an improvement compared to the standard hard pulse-based sequences that had maximum permissible power on a 3-mm inverse cryoprobe, indicating that the UR-180° and UR-90° pulses are efficient transfer elements for the desired rotations, especially at 1.2-GHz ultrahigh-field magnets. These pulses when combined will

retain their performance; hence, a small block in the pulse sequence like INEPT will have a better transfer efficacy, and thus, the entire pulse sequence will have better performance using the OC pulses. The reverse is also true where using the low-power rectangular pulses will lead to the accumulation of pulse imperfections over the blocks resulting in a lower transfer efficacy, and thus, the complete pulse sequence performs poorly, oftentimes with severe phase errors and serious signal losses. We also observe that the more pulses in a sequence, the bigger is the improvement, which is the case for OC-HSQCSI and OC-TROSY when compared to the OC-HSQC experiment. In the case of OC-TROSY, the improvement in the mean S/N is 26.2%, while the improvement seen for OC-HSQC is only 2.7%.

In this work, we demonstrated that the GRAPE algorithm can be used for multiband excitation that produces different nutation angles in each of these bands. Furthermore, the reformulation of multiband selection from the summation of the fidelities for each band to a summation of the system Hamiltonian and the target states can allow combining UR and the PP rotation with different nutation angles per band in a single pulse. To the best of our knowledge, such pulses have not been reported previously, and further studies are necessary to explore the limits of such multiband, multinutation angle pulses. As an immediate application of such pulses, we use a two-band scheme that enables different nutation angles in each band. Thus, we design OC band-selective pulses based on controlling one active (UR-180° or UR-90°) and one inactive (UR-360°) region while leaving the rest of the spectrum uncontrolled. Using this modified scheme, we designed a set of eight different types of low-power OC band-selective pulses that did two-site differential control between the CO spins and the C_α or C_{ali} spins with the controlled active region undergoing a universal rotation. The final pulses had a B_1 inhomogeneity compensation of either ±15 or ±20%, which makes them in practice calibration-free pulses. The variations upon miscalibration result only in a reduction in the enhancement, and even with the maximum miscalibration, we observe a minor enhancement compared to the standard experiments based on hard pulses. The robust reproducibility of these shapes in experiments is due to their smooth phase profiles and the larger B_1 inhomogeneity compensation range. In addition, the careful choice of the excitation profile scheme based on the ^{13}C spin dispersion from the BMRB database allowed us to generate shapes that were shorter for a given power level compared to the previous reports based on the Gaussian shapes. We have demonstrated how these pulses can be easily used in creating a low-power OC version of the 3D-OC-HNCO and 3D-OC-TROSY-HNCO experiments. The conclusions from the low-power 2D experiments are further reinforced by the observed improvements we see in both the 3D experiments. These enhancements we observe now translate as reduced experimental time for attaining a given S/N ratio because the latter depends on the square root of the number of scans and hence the total experimental time (*2*). The expected experimental time is 0.63 times less for OC-TROSY as compared to its hard pulse equivalent to attain the same S/N ratio (table S1). The low-power standard experiments we reported for comparisons are an approximate experimental simulation of the worst-case scenarios for the expected 5-mm inverse cryoprobe. From the extraordinary improvements of more than 240% in S/N ratio, when compared to the low-power standard experiments, we expect the OC sequence to behave robustly even with the limited RF power availability on a 5-mm inverse cryoprobe for a 1.2-GHz spectrometer. It is also evident that the low-power OC sequences developed in this work are immediately useful at 1.2 GHz even on a 3-mm cryoprobe and possibly starting from 1-GHz spectrometers where one can benefit from the S/N ratio enhancements. In such cases where the cryoprobes are not limited by the RF amplitude, it is possible to scale the UR pulses up in power to reduce their durations, which might benefit the studies on large proteins of molecular weight (MW) greater than 40 kDa. With the availability of low-power alternatives for basic building elements, we believe that any bio-NMR experiment can in general be constructed by assembling the OC pulses appropriately. We are working on creating such a low-power OC pulse sequence library to be used for large-volume measurements at the 1.2-GHz spectrometers and the higher ultrahigh-field magnets that are expected to be available in the future.

The major limitation of the above sequences currently is for the application on very large proteins (MW > ~40 kDa), where the relaxation effects would subsume the improvements in the S/N ratio. In addition, there could be potential signal losses in such large systems due to the relatively long duration of the UR-180° and UR-90° pulses when used in 3D sequences. This limitation can be overcome by designing relaxation-compensated OC pulses and sequences (*74*, *75*) or using a shorter PP pulses such as the OPERA (optimizing phase of excitation removes artifacts) (*76*, *77*) or Ramsey-COOP (cooperative) (*24*) type pulses wherever possible. The availability of a reliable pulse shape generator for the NMR instrument is also a limitation in using these OC pulses routinely. In our experience, we have observed that, in general, working with the latest Neo consoles provides the most reliable results for the OC sequences.

In conclusion, we have addressed the low RF power limitation at the 1.2-GHz ultrahigh-field magnets that prevented the use of large-volume probes by designing low-power OC-based sequences. In this work, we designed a set of eight robust low-power UR pulses with an RF amplitude of either 8 or 7.5 kHz on ^1H that covers a bandwidth of 15 or 12.6 kHz and an RF amplitude of 5 kHz on ^{15}N that covers a bandwidth of 6 or 4.8 kHz. The duration of these pulses was from 480 to 700 μs with B_1 inhomogeneity compensation of either ±15 or ±20%. We also generated a set of multiband-selective OC pulses that rotates the spins through different nutation angles in each band. With this scheme and knowledge of chemical shift difference between the ^{13}C spin types in a protein, we do a two-band differential control between the spin types in a protein sample. The above pulses were used to construct low-power OC-based 2D-OC-[^1H,^{15}N]-HSQC, 2D-OC-[^1H,^{15}N]-HSQCSI, 2D-OC-[^1H,^{15}N]-TROSY, 3D-OC-HNCO, and 3D-OC-TROSY-HNCO experiments. All the low-power OC experiments gave an enhanced performance at the 1.2-GHz ultrahigh-field magnet equipped with a 3-mm inverse cryoprobe. Thus, we are confident that these low-power OC-based sequences will enable measurements on the expected 5-mm TCI cryoprobe for the 1.2-GHz instruments. At present, we are creating a library of OC-based bio-NMR pulse sequences for the large-volume measurements at 1.2-GHz spectrometers.

MATERIALS AND METHODS

Numerical optimization and performance simulation of pulse shapes

All the pulse shapes were numerically optimized using the OC module in Spinach v2.5 or v2.7 simulation package based on MATLAB R2020b or R2022b software. Calculations were done on a spin system with N number of noninteracting spins that are evenly spread in the bandwidths of interest. The number of spins N used for optimizing pulses reported in this study are tabulated in tables S3 and S4. We used $M = 121$ number of B_1 fields with linear weights to compensate for B_1 inhomogeneity. The optimization method used was the GRAPE-lbfgs procedure as implemented in Spinach, where the goal was to maximize the real value of the fidelity function in Eq. 1. Other details such as the initial and target states, the bandwidths, the pulse lengths, the RF amplitudes, and the B_1 deviations used for searching the pulse shapes are given in table S3 for all the UR pulses and in table S4 for all the band-selective OC pulses. The initial guess was chosen from 10 randomly generated shapes or a linear combination of sine waves with different frequencies both with 1200 points for discretization, these were optimized systematically by introducing each of the target parameters in steps, and the best among these shapes was chosen for a final optimization. The final shape was smoothened using a moving average filter or DNS penalty as implemented in Spinach.

The spin dynamics simulations on the Bloch sphere and the 2D excitation profiles were calculated by numerically solving the Liouville-von Neumann equation for a single spin

$$\frac{\partial \hat{\sigma}}{\partial t} = -i\,[\hat{\mathrm{H}}, \hat{\sigma}] \tag{8}$$

where the Hamiltonian for time τ during the ith element in OC pulse is given by

$$\hat{\mathrm{H}}(\tau) = \omega_0\ \hat{\mathrm{H}}_{\mathrm{CS}} + c_{i,x}\ \hat{\mathrm{H}}_{\mathrm{rf,x}} + c_{i,y}\ \hat{\mathrm{H}}_{\mathrm{rf,y}} \tag{9}$$

Here, $\hat{H}_{\mathrm{CS}}$ is the chemical shift Hamiltonian and $\hat{H}_{rf,x}$ and $\hat{H}_{rf,y}$ are the x and y components of the pulse Hamiltonian. The density operator after this ith element is given by

$$\hat{\sigma}(\mathrm{t}) = \hat{\mathrm{U}}^{\dagger}(\tau)\ \hat{\sigma}(\mathrm{t} - \tau)\ \hat{\mathrm{U}}(\tau) \tag{10}$$

Here, the propagator is

$$\hat{\mathrm{U}}(\tau) = \exp[-i\hat{\mathrm{H}}(\tau)\tau] \tag{11}$$

The transfer efficacy for the pulse to do a transformation from a state σ_0 to the desired product operator state σ_{targ} for a spin with the nth offset and mth B_1 value from the optimized range is given by Eq. 12

$$\Phi_{n,m}(\sigma_0 \rightarrow \sigma_{\mathrm{targ}}) = Re\ \langle \sigma_{\mathrm{targ}} |\ \prod_i \hat{\mathrm{U}}(\tau)_i\ |\ \sigma_0 \rangle \tag{12}$$

where Π_i represent a Dyson time-ordered series for the discretization of Eq. 1. The pulse shape has steps with duration τ when the pulse Hamiltonian is time invariant. Overall performance index η_{avg} is defined as the trace of the projection of the achieved product operator to the desired product operator averaged over N number of offsets and all the M number of B_1 values for a region of interest.

$$\eta_{\mathrm{avg}} = \frac{\sum_{n,m} \Phi_{n,m}(\sigma_0 \rightarrow \sigma_{\mathrm{targ}})}{(N \times M)} \tag{13}$$

The average expected phase error for a UR pulse is calculated as follows

$$\varphi_{\mathrm{avg}} = \frac{\sum_{n,m} \tan^{-1}\left[\frac{\Phi_{n,m}(\sigma_0 \rightarrow \mathrm{I_y})}{\Phi_{n,m}(\sigma_0 \rightarrow \mathrm{I_x})}\right]}{(N \times M)} \tag{14}$$

Material

The uniformly ^{15}N- and ^{13}C-labeled 2 mM ubiquitin sample in 50 mM sodium phosphate buffer of pH 6.5, containing 100 mM NaCl and 0.1% sodium azide (with 5% D_2O), was used as a test sample to study the performance of all the OC sequences at 1.2 GHz instrument.

NMR measurements

The NMR measurements were performed on an Avance Neo 1200 and 600 MHz Bruker NMR spectrometers at 298 K. The 1200-MHz spectrometer was equipped with a 3-mm TCI cryoprobe, and the 600-MHz spectrometer was equipped with a 5-mm Prodigy cryoprobe. The 90° pulse length on all the three channels was calibrated for the test sample and was used to calculate the power required for OC pulses using the following relation

$$P_{\mathrm{OCP}}\ (\mathrm{dB}) = P_{\mathrm{max}}\ (\mathrm{dB}) - 20\ \log_{10}\left(\frac{\nu_{\mathrm{OCP}}}{\nu_{\mathrm{max}}}\right) \tag{15}$$

Here, ν_{OCP} is the RF amplitude of the OC pulse in kilohertz and $\nu_{\mathrm{max}} = \frac{\omega_{\mathrm{max}}}{2\pi}$ is the calibrated RF amplitude of the hard pulse on a particular channel in kilohertz. The experimental 2D excitation profiles were recorded at the 600neo spectrometer with a sample of 99.9% D_2O doped with 2% $GdCl_3$ to achieve shorter recycle time using a 5-mm Shigemi tube, and the data were acquired as a pseudo-2D spectra with the frequency list in the indirect dimension. The experiments were repeated for 41 or 31 power values corresponding to B_1 deviations and 101 frequency points for UR-180° and UR-90° pulses and with 401 frequency points for OC band-selective pulses. The pseudo-2D data were processed using Topspin 4.0.1 along the direct dimension with the on-resonance, zero-order phase correction, and then the 2D excitation plots were created using a self-written MATLAB code for reading and plotting the processed data.

A 2 mM ubiquitin sample in a 3-mm NMR tube was used to measure the performance of all the low-power OC sequences at the 1200-MHz spectrometer. The important NMR measurement parameters used for acquiring data reported here are tabulated in table S5. The spectra reported were processed using NMRPipe and integrated using PINT software (*78*). All the spectral plots used here were prepared using a self-written MATLAB code for plotting processed data from NMRPipe files. All the reported OC pulses, pulse sequence codes, and the necessary parameter files to reproduce the results on a Bruker Avance Neo 1200 MHz are provided at the Dryad database (doi:10.5061/dryad.g4f4qrfwf).

Supplementary Materials

This PDF file includes:

Figs. S1 to S44
Tables S1 to S5
Optimal control pulse sequences in Bruker format
Legends for movies S1 to S4
Legends for data S1 to S3
Instructions for setting up and acquiring optimal control experiments

Other Supplementary Material for this manuscript includes the following:

Movies S1 to S4
Data S1 to S3

REFERENCES AND NOTES

1. A. Abragam, *The Principles of Nuclear Magnetism* (Oxford Univ. Press, 1983), 618 pp.
2. R. R. Ernst, G. Bodenhausen, A. Wokaun, R. R. Ernst, G. Bodenhausen, A. Wokaun, *Principles of Nuclear Magnetic Resonance in One and Two Dimensions* (Oxford Univ. Press, 1990), 690 pp.
3. J. Cavanagh, N. Skelton, W. Fairbrother, M. Rance, A. Palmer III, *Protein NMR Spectroscopy Principles and Practice* (Elsevier Academic Press, ed. 2, 2007).
4. O. F. Lange, N.-A. Lakomek, C. Farès, G. F. Schröder, K. F. A. Walter, S. Becker, J. Meiler, H. Grubmüller, C. Griesinger, B. L. de Groot, Recognition dynamics up to microseconds revealed from an RDC-derived ubiquitin ensemble in solution. *Science* **320**, 1471–1475 (2008).
5. C. Sanchez-Medina, A. Sekhar, P. Vallurupalli, M. Cerminara, V. Muñoz, L. E. Kay, Probing the free energy landscape of the fast-folding gpW protein by relaxation dispersion NMR. *J. Am. Chem. Soc.* **136**, 7444–7451 (2014).
6. C. Göbl, T. Madl, B. Simon, M. Sattler, NMR approaches for structural analysis of multidomain proteins and complexes in solution. *Prog. Nucl. Magn. Reson. Spectrosc.* **80**, 26–63 (2014).
7. K. S. Chakrabarti, S. Olsson, S. Pratihar, K. Giller, K. Overkamp, K. O. Lee, V. Gapsys, K.-S. Ryu, B. L. de Groot, F. Noé, S. Becker, D. Lee, T. R. Weikl, C. Griesinger, A litmus test for classifying recognition mechanisms of transiently binding proteins. *Nat. Commun.* **13**, 3792 (2022).
8. K. Wüthrich, Protein structure determination in solution by NMR spectroscopy. *J. Biol. Chem.* **265**, 22059–22062 (1990).
9. A. Cavalli, X. Salvatella, C. M. Dobson, M. Vendruscolo, Protein structure determination from NMR chemical shifts. *Proc. Natl. Acad. Sci U.S.A.* **104**, 9615–9620 (2007).
10. R. Sprangers, L. E. Kay, Quantitative dynamics and binding studies of the 20S proteasome by NMR. *Nature* **445**, 618–622 (2007).
11. J. Rinnenthal, J. Buck, J. Ferner, A. Wacker, B. Fürtig, H. Schwalbe, Mapping the landscape of RNA dynamics with NMR spectroscopy. *Acc. Chem. Res.* **44**, 1292–1301 (2011).
12. H. Shi, A. Rangadurai, H. Abou Assi, R. Roy, D. A. Case, D. Herschlag, J. D. Yesselman, H. M. Al-Hashimi, Rapid and accurate determination of atomistic RNA dynamic ensemble models using NMR and structure prediction. *Nat. Commun.* **11**, 5531 (2020).
13. G. Abramov, A. Velyvis, E. Rennella, L. E. Wong, L. E. Kay, A methyl-TROSY approach for NMR studies of high-molecular-weight DNA with application to the nucleosome core particle. *Proc. Natl. Acad. Sci U.S.A.* **117**, 12836–12846 (2020).
14. J. G. Omichinski, G. M. Clore, O. Schaad, G. Felsenfeld, C. Trainor, E. Appella, S. J. Stahl, A. M. Gronenborn, NMR structure of a specific DNA complex of Zn-containing DNA binding domain of GATA-1. *Science* **261**, 438–446 (1993).
15. F.-X. Theillet, In-cell structural biology by NMR: The benefits of the atomic scale. *Chem. Rev.* **122**, 9497–9570 (2022).
16. S. Gil, T. Hošek, Z. Solyom, R. Kümmerle, B. Brutscher, R. Pierattelli, I. C. Felli, NMR spectroscopic studies of intrinsically disordered proteins at near-physiological conditions. *Angew. Chem. Int. Ed.* **52**, 11808–11812 (2013).
17. J.-H. Ardenkjaer-Larsen, G. S. Boebinger, A. Comment, S. Duckett, A. S. Edison, F. Engelke, C. Griesinger, R. G. Griffin, C. Hilty, H. Maeda, G. Parigi, T. Prisner, E. Ravera, J. van Bentum, S. Vega, A. Webb, C. Luchinat, H. Schwalbe, L. Frydman, Facing and overcoming sensitivity challenges in biomolecular NMR spectroscopy. *Angew. Chem. Int. Ed.* **54**, 9162–9185 (2015).
18. D. Joseph, S. Sukumaran, K. Chandra, S. M. Pudakalakatti, A. Dubey, A. Singh, H. S. Atreya, Rapid nuclear magnetic resonance data acquisition with improved resolution and sensitivity for high-throughput metabolomic analysis. *Magn. Reson. Chem.* **59**, 300–314 (2021).
19. P. Wikus, W. Frantz, R. Kümmerle, P. Vonlanthen, Commercial gigahertz-class NMR magnets. *Supercond. Sci. Technol.* **35**, 033001 (2022).
20. H. Schwalbe, Editorial: New 1.2 GHz NMR spectrometers—New horizons? *Angew. Chem. Int. Ed. Engl.* **56**, 10252–10253 (2017).
21. E. Nimerovsky, K. T. Movellan, X. C. Zhang, M. C. Forster, E. Najbauer, K. Xue, R. Dervişoğlu, K. Giller, C. Griesinger, S. Becker, L. B. Andreas, Proton detected solid-state NMR of membrane proteins at 28 Tesla (1.2 GHz) and 100 kHz magic-angle spinning. *Biomolecules* **11**, 752 (2021).
22. M. Callon, A. A. Malär, S. Pfister, V. Římal, M. E. Weber, T. Wiegand, J. Zehnder, M. Chávez, R. Cadalbert, R. Deb, A. Däpp, M.-L. Fogeron, A. Hunkeler, L. Lecoq, A. Torosyan, D. Zyla, R. Glockshuber, S. Jonas, M. Nassal, M. Ernst, A. Böckmann, B. H. Meier, Biomolecular solid-state NMR spectroscopy at 1200 MHz: The gain in resolution. *J. Biomol. NMR* **75**, 255–272 (2021).
23. E. Luchinat, L. Barbieri, M. Cremonini, L. Banci, Protein in-cell NMR spectroscopy at 1.2 GHz. *J. Biomol. NMR* **75**, 97–107 (2021).
24. S. Asami, W. Kallies, J. C. Günther, M. Stavropoulou, S. J. Glaser, M. Sattler, Ultrashort broadband cooperative pulses for multidimensional biomolecular NMR experiments. *Angew. Chem. Int. Ed.* **57**, 14498–14502 (2018).
25. P. F. Flynn, D. L. Mattiello, H. D. W. Hill, A. J. Wand, Optimal use of cryogenic probe technology in NMR studies of proteins. *J. Am. Chem. Soc.* **122**, 4823–4824 (2000).
26. L. C. Robosky, M. D. Reily, D. Avizonis, Improving NMR sensitivity by use of salt-tolerant cryogenically cooled probes. *Anal. Bioanal. Chem.* **387**, 529–532 (2007).
27. G. W. Clark, Pulsed nuclear resonance apparatus. *Rev. Sci. Instrum.* **35**, 316–333 (1964).
28. D. D. Wheeler, M. S. Conradi, Practical exercises for learning to construct NMR/MRI probe circuits. *Concepts Magn. Reson.* **40A**, 1–13 (2012).
29. M. W. Voehler, G. Collier, J. K. Young, M. P. Stone, M. W. Germann, Performance of cryogenic probes as a function of ionic strength and sample tube geometry. *J. Magn. Reson.* **183**, 102–109 (2006).
30. S. J. Glaser, T. Schulte-Herbrüggen, M. Sieveking, O. Schedletzky, N. C. Nielsen, O. W. Sørensen, C. Griesinger, Unitary control in quantum ensembles: Maximizing signal intensity in coherent spectroscopy. *Science* **280**, 421–424 (1998).
31. N. Khaneja, "Geometric control in classical and quantum systems," thesis, Harvard University, Cambridge, MA (2000).
32. N. Khaneja, S. Glaser, R. Brockett, Subriemannian geodesics and optimal control of spin systems, in *Proceedings of the 2002 American Control Conference* (IEEE, 2002), vol. 4, pp. 2806–2811.
33. N. Khaneja, S. J. Glaser, R. Brockett, Sub-Riemannian geometry and time optimal control of three spin systems: Quantum gates and coherence transfer. *Phys. Rev. A* **65**, 032301 (2002).
34. N. Khaneja, R. Brockett, S. J. Glaser, Time optimal control in spin systems. *Phys. Rev. A* **63**, 032308 (2001).
35. T. O. Reiss, N. Khaneja, S. J. Glaser, Time-optimal coherence-order-selective transfer of in-phase coherence in heteronuclear IS spin systems. *J. Magn. Reson.* **154**, 192–195 (2002).
36. N. C. Nielsen, C. Kehlet, S. J. Glaser, N. Khaneja, Optimal control methods in NMR spectroscopy. *eMagRes* (2010).
37. N. Khaneja, T. Reiss, C. Kehlet, T. Schulte-Herbrüggen, S. J. Glaser, Optimal control of coupled spin dynamics: Design of NMR pulse sequences by gradient ascent algorithms. *J. Magn. Reson.* **172**, 296–305 (2005).
38. Z. Tošner, T. Vosegaard, C. Kehlet, N. Khaneja, S. J. Glaser, N. C. Nielsen, Optimal control in NMR spectroscopy: Numerical implementation in SIMPSON. *J. Magn. Reson.* **197**, 120–134 (2009).
39. I. Kuprov, Optimal control of spin systems, in *Spin: From Basic Symmetries to Quantum Optimal Control* (Springer International Publishing, 2023), pp. 313–349.
40. T. E. Skinner, T. O. Reiss, B. Luy, N. Khaneja, S. J. Glaser, Application of optimal control theory to the design of broadband excitation pulses for high-resolution NMR. *J. Magn. Reson.* **163**, 8–15 (2003).
41. K. Kobzar, T. E. Skinner, N. Khaneja, S. J. Glaser, B. Luy, Exploring the limits of broadband excitation and inversion pulses. *J. Magn. Reson.* **170**, 236–243 (2004).
42. K. Kobzar, T. E. Skinner, N. Khaneja, S. J. Glaser, B. Luy, Exploring the limits of broadband excitation and inversion: II. RF-power optimized pulses. *J. Magn. Reson.* **194**, 58–66 (2008).
43. K. Kobzar, S. Ehni, T. E. Skinner, S. J. Glaser, B. Luy, Exploring the limits of broadband 90° and 180° universal rotation pulses. *J. Magn. Reson.* **225**, 142–160 (2012).
44. T. E. Skinner, T. O. Reiss, B. Luy, N. Khaneja, S. J. Glaser, Reducing the duration of broadband excitation pulses using optimal control with limited RF amplitude. *J. Magn. Reson.* **167**, 68–74 (2004).
45. T. E. Skinner, K. Kobzar, B. Luy, M. R. Bendall, W. Bermel, N. Khaneja, S. J. Glaser, Optimal control design of constant amplitude phase-modulated pulses: Application to calibration-free broadband excitation. *J. Magn. Reson.* **179**, 241–249 (2006).
46. H. J. Hogben, M. Krzystyniak, G. T. P. Charnock, P. J. Hore, I. Kuprov, Spinach – A software library for simulation of spin dynamics in large spin systems. *J. Magn. Reson.* **208**, 179–194 (2011).

47. D. L. Goodwin, I. Kuprov, Modified Newton-Raphson GRAPE methods for optimal control of spin systems. *J. Chem. Phys.* **144**, 204107 (2016).
48. D. L. Goodwin, I. Kuprov, Auxiliary matrix formalism for interaction representation transformations, optimal control, and spin relaxation theories. *J. Chem. Phys.* **143**, 084113 (2015).
49. P. de Fouquieres, S. G. Schirmer, S. J. Glaser, I. Kuprov, Second order gradient ascent pulse engineering. *J. Magn. Reson.* **212**, 412–417 (2011).
50. S. Ehni, B. Luy, BEBEtr and BUBI: J-compensated concurrent shaped pulses for 1H–13C experiments. *J. Magn. Reson.* **232**, 7–17 (2013).
51. M. Nimbalkar, B. Luy, T. E. Skinner, J. L. Neves, N. I. Gershenzon, K. Kobzar, W. Bermel, S. J. Glaser, The fantastic four: A plug 'n' play set of optimal control pulses for enhancing NMR spectroscopy. *J. Magn. Reson.* **228**, 16–31 (2013).
52. G. Rancan, T. T. Nguyen, S. J. Glaser, Gradient ascent pulse engineering for rapid exchange saturation transfer. *J. Magn. Reson.* **252**, 1–9 (2015).
53. A. Lingel, A. Vulpetti, T. Reinsperger, A. Proudfoot, R. Denay, A. Frommlet, C. Henry, U. Hommel, A. D. Gossert, B. Luy, A. O. Frank, Comprehensive and high-throughput exploration of chemical space using broadband ^{19}F NMR-based screening. *Angew. Chem. Int. Ed.* **59**, 14809–14817 (2020).
54. P. W. Coote, S. A. Robson, A. Dubey, A. Boeszoermenyi, M. Zhao, G. Wagner, H. Arthanari, Optimal control theory enables homonuclear decoupling without Bloch–Siegert shifts in NMR spectroscopy. *Nat. Commun.* **9**, 3014 (2018).
55. F. Schilling, L. R. Warner, N. I. Gershenzon, T. E. Skinner, M. Sattler, S. J. Glaser, Next-generation heteronuclear decoupling for high-field biomolecular NMR spectroscopy. *Angew. Chem. Int. Ed.* **53**, 4475–4479 (2014).
56. T. E. Skinner, N. I. Gershenzon, M. Nimbalkar, S. J. Glaser, Optimal control design of band-selective excitation pulses that accommodate relaxation and RF inhomogeneity. *J. Magn. Reson.* **217**, 53–60 (2012).
57. S. Slad, W. Bermel, R. Kümmerle, D. Mathieu, B. Luy, Band-selective universal 90° and 180° rotation pulses covering the aliphatic carbon chemical shift range for triple resonance experiments on 1.2 GHz spectrometers. *J. Biomol. NMR* **76**, 185–195 (2022).
58. C. Kehlet, M. Bjerring, A. C. Sivertsen, T. Kristensen, J. J. Enghild, S. J. Glaser, N. Khaneja, N. C. Nielsen, Optimal control based NCO and NCA experiments for spectral assignment in biological solid-state NMR spectroscopy. *J. Magn. Reson.* **188**, 216–230 (2007).
59. T. Vosegaard, C. Kehlet, N. Khaneja, S. J. Glaser, N. C. Nielsen, Improved excitation schemes for multiple-quantum magic-angle spinning for quadrupolar nuclei designed using optimal control theory. *J. Am. Chem. Soc.* **127**, 13768–13769 (2005).
60. Z. Tošner, M. J. Brandl, J. Blahut, S. J. Glaser, B. Reif, Maximizing efficiency of dipolar recoupling in solid-state NMR using optimal control sequences. *Sci. Adv.* **7**, eabj5913 (2021).
61. J. Blahut, M. J. Brandl, T. Pradhan, B. Reif, Z. Tošner, Sensitivity-enhanced multidimensional solid-state NMR spectroscopy by optimal-control-based transverse mixing sequences. *J. Am. Chem. Soc.* **144**, 17336–17340 (2022).
62. J. C. Saywell, I. Kuprov, D. Goodwin, M. Carey, T. Freegarde, Optimal control of mirror pulses for cold-atom interferometry. *Phys. Rev. A* **98**, 023625 (2018).
63. J. Saywell, M. Carey, M. Belal, I. Kuprov, T. Freegarde, Optimal control of Raman pulse sequences for atom interferometry. *J. Phys. B At. Mol. Opt. Phys.* **53**, 085006 (2020).
64. J. Saywell, M. Carey, I. Kuprov, T. Freegarde, Biselective pulses for large-area atom interferometry. *Phys. Rev. A* **101**, 063625 (2020).
65. G. A. Morris, R. Freeman, Enhancement of nuclear magnetic resonance signals by polarization transfer. *J. Am. Chem. Soc.* **101**, 760–762 (1979).
66. R. Freeman, Shaped radiofrequency pulses in high resolution NMR. *Prog. Nucl. Magn. Reson. Spectrosc.* **32**, 59–106 (1998).
67. M. Sattler, J. Schleucher, C. Griesinger, Heteronuclear multidimensional NMR experiments for the structure determination of proteins in solution employing pulsed field gradients. *Prog. Nucl. Magn. Reson. Spectrosc.* **34**, 93–158 (1999).
68. L. Emsley, G. Bodenhausen, Gaussian pulse cascades: New analytical functions for rectangular selective inversion and in-phase excitation in NMR. *Chem. Phys. Lett.* **165**, 469–476 (1990).
69. L. Emsley, G. Bodenhausen, Optimization of shaped selective pulses for NMR using a quaternion description of their overall propagators. *J. Magn. Reson.* **97**, 135–148 (1992).
70. H. Geen, R. Freeman, Band-selective radiofrequency pulses. *J. Magn. Reson.* **93**, 93–141 (1991).
71. D. L. Goodwin, "Advanced optimal control methods for spin systems," thesis, University of Southampton, Southampton, UK (2017).
72. I. Kuprov, Spin system trajectory analysis under optimal control pulses. *J. Magn. Reson.* **233**, 107–112 (2013).
73. Ě. Kuře, R. Freeman, Frequency-domain Hadamard spectroscopy. *J. Magn. Reson.* **162**, 158–165 (2003).
74. N. Khaneja, T. Reiss, B. Luy, S. J. Glaser, Optimal control of spin dynamics in the presence of relaxation. *J. Magn. Reson.* **162**, 311–319 (2003).
75. D. P. Frueh, T. Ito, J.-S. Li, G. Wagner, S. J. Glaser, N. Khaneja, Sensitivity enhancement in NMR of macromolecules by application of optimal control theory. *J. Biomol. NMR* **32**, 23–30 (2005).
76. P. Coote, W. Bermel, H. Arthanari, Optimization of phase dispersion enables broadband excitation without homonuclear coupling artifacts. *J. Magn. Reson.* **325**, 106928 (2021).
77. P. Coote, C. Anklin, W. Massefski, G. Wagner, H. Arthanari, Rapid convergence of optimal control in NMR using numerically-constructed toggling frames. *J. Magn. Reson.* **281**, 94–103 (2017).
78. M. Niklasson, R. Otten, A. Ahlner, C. Andresen, J. Schlagnitweit, K. Petzold, P. Lundström, Comprehensive analysis of NMR data using advanced line shape fitting. *J. Biomol. NMR* **69**, 93–99 (2017).

Acknowledgments: We thank S. Becker and M. Wegstroth for providing the isotopically labeled ubiquitin sample and D. Bockelmann for assistance with setting up software on Linux servers. We also thank I. Kuprov for discussions on the Spinach package, R. Kümmerle and W. Bermel for discussion on the expected maximum RF amplitudes of a 5-mm cryoprobe, and P. W. Coote and H. Arthanari on optimal control pulses in general. **Funding:** This work was supported by the Max Planck Society. **Author contributions:** C.G. conceptualized the problem. D.J. and C.G. designed the study. D.J. optimized the pulses, constructed the pulses sequences, and carried out the simulation and experiments. D.J. interpreted the data and wrote the initial draft. D.J. and C.G. reviewed and edited the manuscript. **Competing interests:** The authors declare that they have no competing interests. **Data and materials availability:** All data needed to evaluate the conclusions in the paper are present in the paper and/or the Supplementary Materials. All the reported OC pulses, pulse sequence codes, and the necessary parameter files to reproduce the results on a Bruker Avance Neo 1200 MHz are provided at the Dryad database as "Data S1 to S3 from the manuscript Optimal control pulses for the 1.2 GHz (28.2 T) NMR spectrometers" (doi:10.5061/dryad.g4f4qrfwf).

Submitted 7 June 2023
Accepted 12 October 2023
Published 10 November 2023
10.1126/sciadv.adj1133

ScienceAdvances

Optimal control pulses for the 1.2-GHz (28.2-T) NMR spectrometers

David Joseph and Christian Griesinger

Sci. Adv. **9** (45), eadj1133. DOI: 10.1126/sciadv.adj1133

Science Advances (ISSN 2375-2548) is published by the American Association for the Advancement of Science. 1200 New York Avenue NW, Washington, DC 20005. The title *Science Advances* is a registered trademark of AAAS.